POLITECNICO DI TORINO

Collegio di Ingegneria Chimica e dei Materiali

Master of Science Course
in Materials Engineering for Industry 4.0

Master of Science Thesis

In Situ Control of the Phase and Grain Microstructure of 316L Stainless Steel during Directed Energy Deposition

Politecnico di Torino

Tutors

Prof. Cédric Bosch
Prof. Cédric Courbon
Prof. Daniele Ugues

Candidate

Folco Perego

October 2025

Erasmus Mundus Joint Master in Manufacturing 4.0 by intElligent and susTAinable technologies

MASTER's Degree Thesis

In Situ Control of the Phase and Grain Microstructure of 316L Stainless Steel during Directed Energy Deposition

Supervisors

Prof. Cédric BOSCH

Prof. Cédric COURBON

Prof. Daniele UGUES

Candidate

Folco PEREGO

September 2025

Abstract

Controlling grain structure in metal additive manufacturing (AM) is critical for mitigating anisotropic mechanical behavior caused by columnar grain growth along the build direction. Grain refinement not only reduces hot cracking susceptibility but also enhances mechanical performance via the Hall–Petch effect. This study explores the feasibility of in-situ grain refinement in 316L stainless steel fabricated by Directed Energy Deposition (DED) through the direct injection of titanium (Ti) particles into the melt pool. Unlike premixed powders, which often exhibit non-uniform distribution due to differences in density, morphology, and gas interactions, direct Ti injection provides real-time control over alloying composition and enables local microstructural tailoring.

A systematic parametric study was conducted by varying nozzle velocity (up to 10,000 mm/min), Ti feed rate, and the number of rescanning passes to evaluate their combined effect on microstructure, inclusions, and the transition from coarse columnar grains to fine equiaxed grains. Experimental observations revealed that Ti injection promotes equiaxed grain formation through the precipitation of Ti-rich compounds and a shift in solidification mode within the 316L microstructure.
Complementary Thermo-Calc simulations were used to predict phase stability and inform the process design, ensuring avoidance of brittle Fe–Ti intermetallics. Results indicated that low Ti feed rates refine grains effectively without triggering phase transitions in the austenitic matrix. In contrast, higher Ti additions caused inclusions, cracking, and fully ferritic solidification. Laser rescanning mitigated inclusions and reduced crack formation by homogenizing Ti distribution.

This combined experimental and modeling approach establishes a first framework for microstructural control in 316L DED via optimized Ti injection. The findings demonstrate the potential of this strategy to achieve tailored grain structures, limit anisotropy, and improve reliability in additively manufactured stainless steel components.

Keywords: Additive manufacturing, DED, Grain refinement, Microstructure tailoring, Titanium injection, EBSD.

Acknowledgments

The work presented in this thesis was carried out at the Swiss Federal Laboratories for Materials Science and Technology (Empa), within the Advanced Processing and Additive Manufacturing of Metals group, from March to August 2025.

First and foremost, I would like to express my deepest gratitude to my supervisor, Dr. Christian Leinenbach, for granting me the invaluable opportunity to pursue my final project within his research group. His guidance, expertise, and unwavering support have been fundamental to both my professional and personal growth. I am especially grateful for the countless hours he dedicated to discussions, reviewing drafts, and providing insightful feedback, all of which have significantly enhanced the quality of this work. I would also like to extend my sincere appreciation to all collaborators who contributed to this project. In particular, I am indebted to Dr. Akash Aggarwal, Dr. Marc Leparoux, Prof. Cedric Bosch, Prof. Helmut Klocker and Dr. Antonios Baganis for their invaluable input and continuous support throughout this research. I am equally thankful to my colleagues, Abdullah, Abhijith, Davi, Gustavo, Muteeb, Patrycja and many others, with whom I shared not only professional collaboration but also enduring friendships that greatly enriched this experience.

Finally, I wish to thank my family and Brittney for their unwavering patience, encouragement, and understanding. Their support has been my greatest source of strength and motivation throughout this journey. I feel truly blessed to have such wonderful people by my side, and I am deeply grateful for their love.

In science, if you know what you are doing, you should not be doing it.
In engineering, if you do not know what you are doing, you should not be doing it.
- Richard Hamming

Table of Contents

List of Figures

List of Tables

Nomenclature

Abbreviations & acronyms

SE	Standard Error
A	Austenitic
A-SS	Austenitic Stainless Steel
AF	Austenitic-Ferritic
AM	Additive Manufacturing
BCC	Body Centered Cubic
BSE	Backscattered Electron
CET	Columnar to Equiaxed Transition
CLAHE	Contrast Limited Adaptive Histogram Equalization
CTE	Coefficient of Thermal Expansion
EBM	Electron Beam Melting
EBSD	Electron Back Scatter Diffraction
EDS	Energy Dispersive X-ray Spectroscopy
F	Ferritic
FA	Ferritic-Austenitic
FCC	Face Centered Cubic
HRTEM	High-Resolution Transmission Electron Microscopy
IPF	Inverted Pole Figure
L-DED	Laser Directed Energy Deposition
L-PBF	Laser Powder Bed Fusion
LEI	Linear Energy Input
LOM	Light Optical Microscopy
NV	Nozzle Velocity

R	Number of Rescanning Passes
ROI	Region of Interest
S-G	Scheil-Gulliver
S/L	Solid-liquid
SAED	Selected Area Electron Diffraction
SE	Secondary Electron
SEM	Scanning Electron Microscope
Ti FR	Titanium Injection Feed Rate
TiN	Titanium Nitride

Other symbols

ΔS_v	Entropy of phase transition per unit volume
ΔT	Total undercooling
ΔT_n	Critical nucleation undercooling
ΔT_t	Thermal undercooling
ΔT_{CS}	Constitutional supercooling
δ	Lattice misfit between nucleant particle and solid grain
$\dot{T}$	Cooling rate
We	Weber number
ρ^*	Dimensionless density ratio
ρ_g	Density of gas
ρ_l	Density of liquid
ρ_s	Density of solid
σ	Surface tension
α	Absorptivity
δ	Ferrite
L	Liquid

Θ	Liquid–solid contact angle
C_0	Solute concentration
c_E	Elastic constant related to interfacial energy
G	Thermal gradient
g	Gravitational acceleration
K_d	Growth kinetics coefficient
m	Liquidus line slope
n	Material constant
N_0	Number of active nucleation sites
P	Laser Power
Q	Growth restriction factor
R	Solidification rate
r	Particle radius
T_L	Liquidus temperature
T_M	Melt temperature
u	Carrying gas velocity
v	Particle impact velocity
V_{NV}	Nozzle speed
ϕ	Volume fraction of pre-formed equiaxed grains
γ	Austenite

Chapter 1

Introduction

Additive Manufacturing (AM) has undergone significant advancement in recent years, with origins in the stereolithography techniques developed by Charles Hull in the 1980s. [1]. Unlike traditional subtractive manufacturing methods such as machining, AM constructs components layer-by-layer from a digital model. This paradigm shift enables the fabrication of complex geometries with minimal material waste. AM now supports a broad range of materials, including polymers, metals, ceramics, and even food, underscoring its versatility in modern manufacturing. The sustainability potential of AM is also substantial, as it can enhance energy efficiency and drastically reduce material waste when compared with conventional manufacturing methods. Various classification schemes exist for AM processes; however, the most widely adopted categorization is based on the form of the feedstock material, as illustrated in Fig. 1.1. The selection of a suitable AM technique depends on several factors, including build volume, required resolution and surface quality, production rate, and the type of energy source utilized [2].

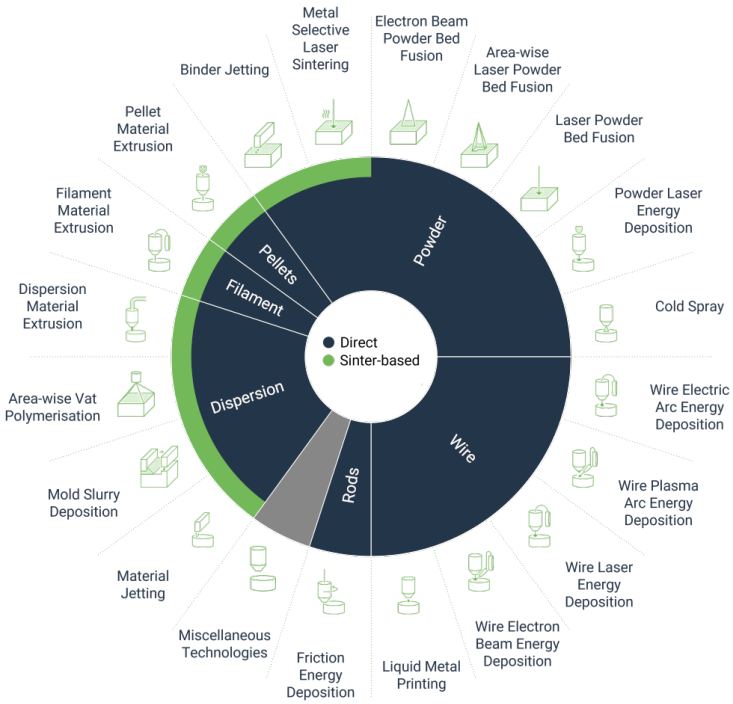

Figure 1.1: Feedstock-based classification of AM technologies [3].

Among the various metal AM techniques, those employing powder-based feedstocks are the most widely used. In Powder Bed Fusion processes, such as Laser PBF (L-PBF) or Electron Beam Melting (EBM), a focused energy source selectively fuses regions of a powder bed layer-by-layer as shown in the schematics of Fig. 1.2(a,b). These are considered direct metal AM technologies and are among the most extensively studied. Figure 1.1 includes other sinter-based methods, like Binder Jetting (Fig. 1.2(c)), in which a polymer binder is deposited onto a powder bed to hold the material into a 'green' part, which is later sintered to achieve full density.

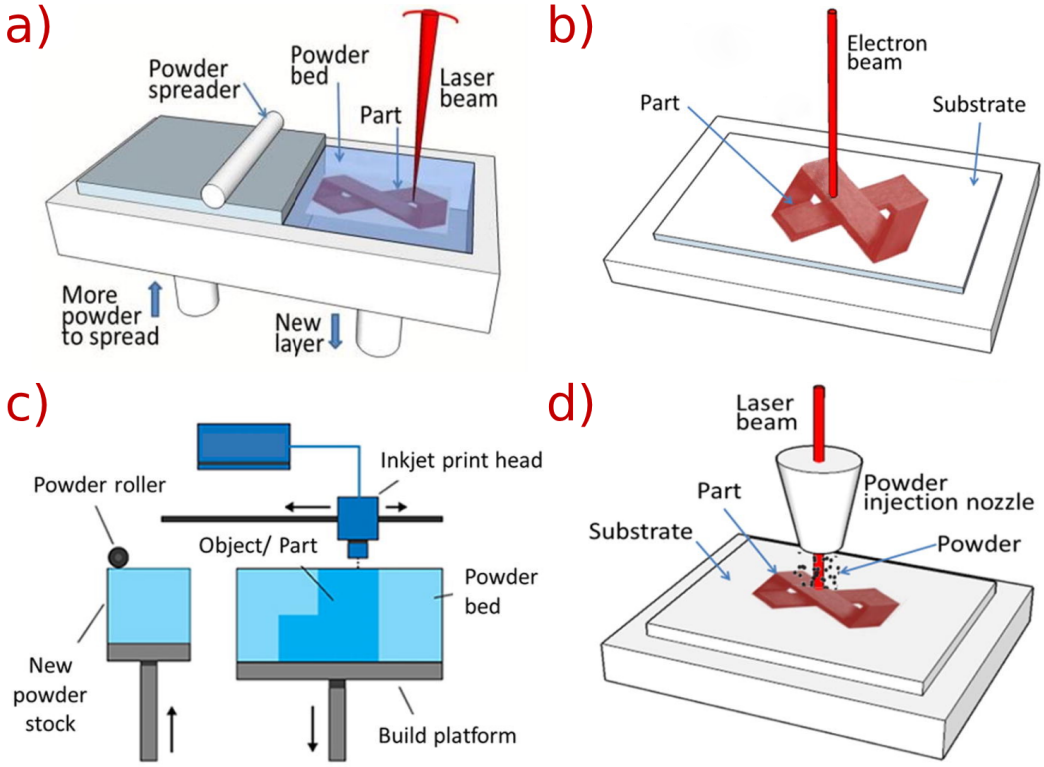

Figure 1.2: Schematic diagram of (a) L-PBF, (b) EBM, (c) Binder Jetting, and (d) DED process. Adapted from DebRoy et al. [4].

Conversely, Directed Energy Deposition (DED) does not rely on a powder bed as the powder or wire feedstock is delivered directly into a melt pool generated by a focused energy source, such as a laser, electron beam, or plasma arc as shown in the Fig. 1.2(d) schematic. The melt pool rapidly solidifies to form a deposit track or clad layer on the substrate [5].

Laser Directed Energy Deposition (L-DED), also known as laser metal deposition or more commonly laser cladding, utilizes laser welding techniques to deposit a wire or powder feedstock onto a metallic substrate. Generally, powder feed systems are em-

ployed to manufacture near-net-shaped small to medium-sized parts. In contrast, wire feed systems are preferred for creating components with low to medium complexity and medium to large dimensions. Fig. 1.3 depicts two examples of powder and wire-based L-DED side by side.

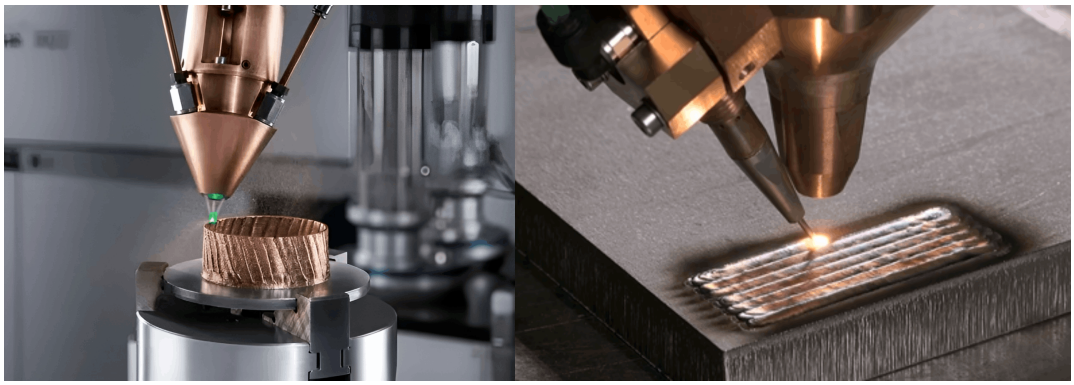

Figure 1.3: Powder and wire-based L-DED systems respectively.

To contextualize the role of L-DED, hereafter referred to as DED, within the metal AM landscape, it is helpful to compare it with the more extensively studied L-PBF. Unlike L-PBF, where powder is spread layer by layer before fusion, DED continuously supplies feedstock directly to the melt pool. Key industrial advantages of DED over L-PBF include:

- Capability to fabricate large-scale components up to several meters and weights of hundreds of kilograms, while L-PBF is limited to build volumes $\leq 0.03 m^3$ due to its enclosed chamber design [2],
- Higher deposition rates, reduced lead times and improved productivity [6],
- Greater feedstock flexibility, as DED can utilize powder, wire, or rod, whereas L-PBF is restricted to powders.

Moreover, the minimal presence of powder inside the building chamber and the possibility of attaching multiple hoppers at the inlet allow for the fabrication of a broad range of materials with minimal housekeeping, unlike L-PBF, which requires extensive cleaning when switching between alloy systems. The absence of a powder bed also significantly reduces material consumption, offering cost advantages, particularly for expensive alloys containing refractory elements.
However, DED presents several limitations when compared to L-PBF:

- Larger melt pool size, increased layer thickness, and wider hatch spacing make DED less suitable for fabricating fine, intricate geometries [4],
- Lower relative density of DED-fabricated parts,

- Reduced dimensional accuracy and increased surface roughness, requiring post-processing [7].

Nevertheless, the use of localized shielding gas in DED enables processing in environments that do not require a fully inert atmosphere, facilitating unique capabilities such as underwater printing [8]. Additionally, since microstructural evolution during solidification is primarily governed by process parameters rather than feedstock morphology, DED allows for significant microstructural tailoring.
Historically used for cladding and repair applications [5], DED is also well suited for fabricating functionally graded materials by mixing different alloys in the feed system [9, 10]. Gradients in composition, microstructure, and properties can be achieved by dynamically adjusting feedstock ratios and process parameters [11]. Manipulating the processing conditions can enable the creation of specific microstructures engineered for designed properties.

Recent advances in AM include the fabrication of Damascus-like steel structures by Kürnsteiner et al. [12], where controlled cooling was applied to produce alternating hard and soft layers in a Fe–19Ni–5Ti system. Likewise, Todaro et al. [13] demonstrated that the application of high-intensity ultrasound during powder-based DED can effectively manipulate grain growth in Ti-6Al-4V and transition from columnar to fine equiaxed grains, thereby enhancing mechanical performance. Unlike powder bed fusion processes, DED offers direct access to the melt pool, creating unique opportunities for implementing in-situ microstructural tailoring and grain refinement strategies. Building on these developments, the present study investigates the feasibility of locally modifying the 316L microstructure through the injection of titanium particles during DED, with the rationale for this approach detailed in the following chapter.

Chapter 2

Microstructure Tailoring in Steel DED

This chapter will provide a brief overview of the primary applications of 316L stainless steel in DED, as well as the state-of-the-art techniques employed for microstructural tailoring. The approaches presented represent the most relevant strategies, but are not intended as an exhaustive review of microstructure design. Traditionally, grain refinement in metallic materials has been achieved through severe plastic deformation techniques, such as cold rolling, equal-channel angular pressing, or dynamic plastic deformation under high strain rates [14]. While effective, these methods are not directly applicable to DED manufactured components, which often feature complex geometries that cannot accommodate such post-processing techniques.

2.1 316L Stainless Steel in DED

The 316L stainless steel grade is the second most widely used austenitic stainless steel (A-SS), following 304L. As reported by Kerner et al. [15], the addition of molybdenum enhances its corrosion resistance relative to 304L. Owing to its high strength, thermal stability, and excellent corrosion resistance in aggressive environments, 316L is extensively employed in nuclear reactors, boilers, pipelines, heat exchangers, furnaces, and across the oil, gas, and chemical industries [16]. These applications highlight 316L as a promising candidate for the cost-effective repair capabilities of DED, which offers advantages such as fabricating complex geometries, accommodating large build volumes, and locally tailoring microstructures for demanding service conditions (e.g., high-temperature oxidation, tribology, or corrosion resistance).

2.1.1 Main challenges

Despite these advantages, several limitations remain:

- Limited geometric precision (typically $\pm$ 0.2 mm) restricts as-built applications.
- Accumulated thermal cycles induce residual stress and geometric distortions [16].
- Directional thermal gradients during deposition promote a highly textured microstructure, resulting in anisotropic mechanical behavior.

The latter challenge is particularly difficult to overcome, as the inherent characteristics of the DED process favor epitaxial solidification, a phenomenon commonly observed

across alloys processed by AM [4, 17]. In such cases, the solidifying grains grow parallel to the thermal gradient (G) with a growth rate (R) determined by the scan speed [17]. The resulting columnar grains, illustrated in Fig. 2.1, can negatively affect mechanical performance.

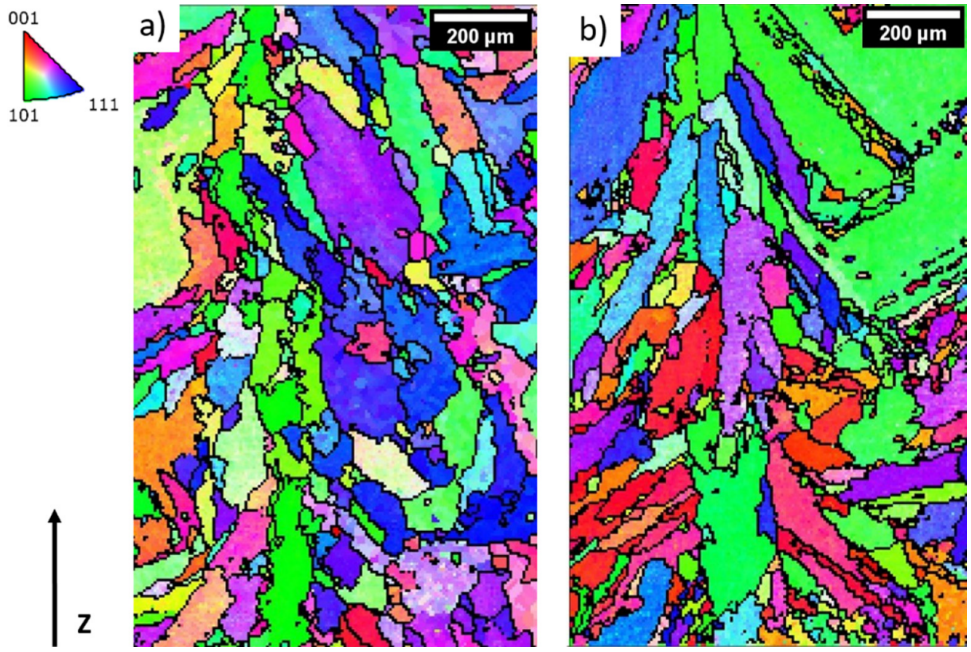

Figure 2.1: Inverse pole figure (IPF) maps of 316L samples fabricated with Z as the building direction using (a) low power and (b) high power parameters [17].

Their elongated morphology and crystallographic orientation influence how the material deforms under stress, as loading parallel to the grain boundaries encounters less resistance than loading perpendicular to them. These anisotropic features create a direction-dependent response with variations in strength and ductility depending on the grain morphology and loading direction, known as mechanical anisotropy. While anisotropy can be functionalized for specific applications, when combined with the complex geometries of the DED components, it could negatively affect the tensile and fatigue behavior [4].

The effects of processing parameters on additively manufactured A-SS have been widely studied [2, 4, 5, 7, 11, 13, 17, 18] to mitigate defects and obtain the desired properties. Increasingly, research is shifting toward strategies that locally tailor material properties and reduce anisotropy by controlling the solidified microstructure. For example, Gao et al. [19] demonstrated that modifying deposition strategies in wire-based DED can reduce anisotropy and enhance ductility. Similarly, Wang et al. [20] and Tan et al. [21] showed that the addition of titanium nitride (TiN) nanoparticles to 316 stainless steel significantly refines grains, promotes more uniform tensile deformation, and improves

strength–ductility performance. As illustrated in Fig. 2.2, the non-inoculated 316L alloy (Fig. 2.2(a)) exhibits epitaxial columnar grains oriented close to $\langle 100 \rangle$. With 2 wt.% TiN addition, the grain size is markedly refined and the morphology transitions to near-equiaxed (Fig. 2.2(b)). Increasing the TiN addition to 4 wt.% further enhances equiaxed refinement and produces a more uniform structure (Fig. 2.2(c)). However, at 6 wt.% TiN no additional refinement is observed (Fig. 2.2(d)). The varied colors across the 2–6 wt.% TiN samples reflect random crystallographic texture [20].

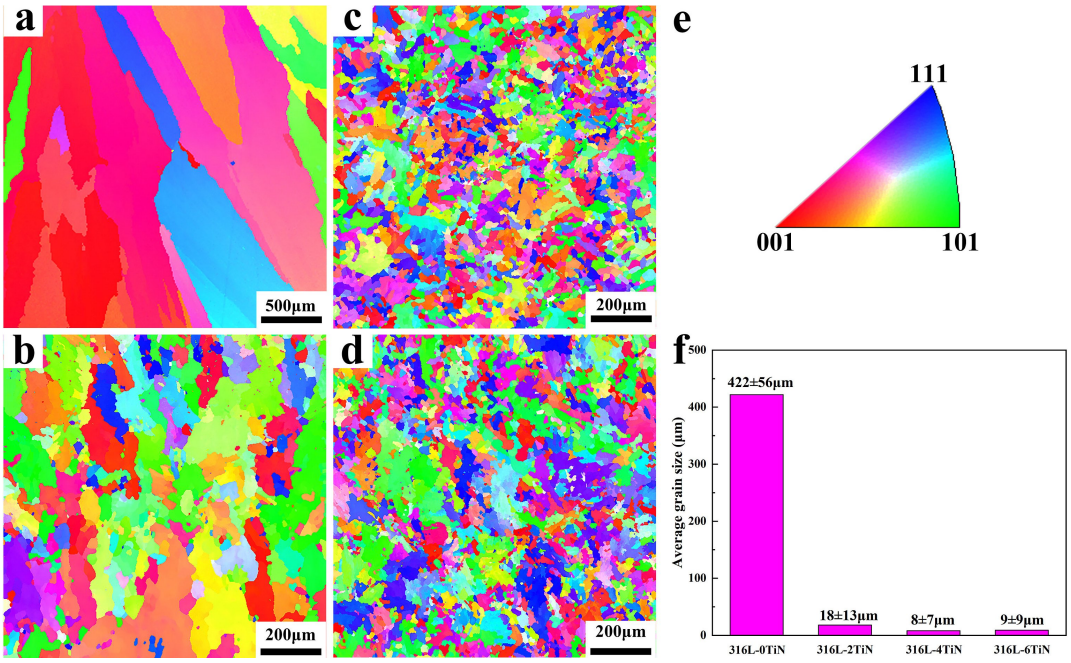

Figure 2.2: EBSD orientation maps of (a) 316L-0TiN, (b) 316L-2TiN, (c) 316L-4TiN, and (d) 316L-6TiN. (e) Definition of colors with respect to crystal orientation in maps (a–d). (f) Sample average grain size. Note: in (f) the grain size for 316L-0TiN represents the average width of columnar grains [20].

The mechanical response is shown in the engineering stress–strain curves in Fig. 2.3, where the transverse and longitudinal samples correspond to Fig. 2.3(a) and (b), respectively. The sample orientation relative to the build direction is indicated in the schematic. The 316L-0TiN sample exhibits anisotropic mechanical properties, with lower strength, but higher elongation in the longitudinal compared to the transverse direction. This behavior stems from the columnar grain structure seen in Fig. 2.1 and Fig. 2.2(a). The specimens deformed along the build direction contain fewer grain boundaries than those deformed transversely. According to Hall–Petch strengthening, the higher grain boundary density in the transverse samples increases strength, but at the cost of ductility, as grain boundaries act as potential crack initiation sites [20, 21, 22].

With TiN additions, the samples exhibit nearly isotropic mechanical properties due to

the equiaxed grain morphology. TiN additions increase both yield and tensile strength; however, they reduce elongation, particularly at 4 wt.% TiN. A balanced combination of strength and ductility is achieved at 2 wt.% TiN.

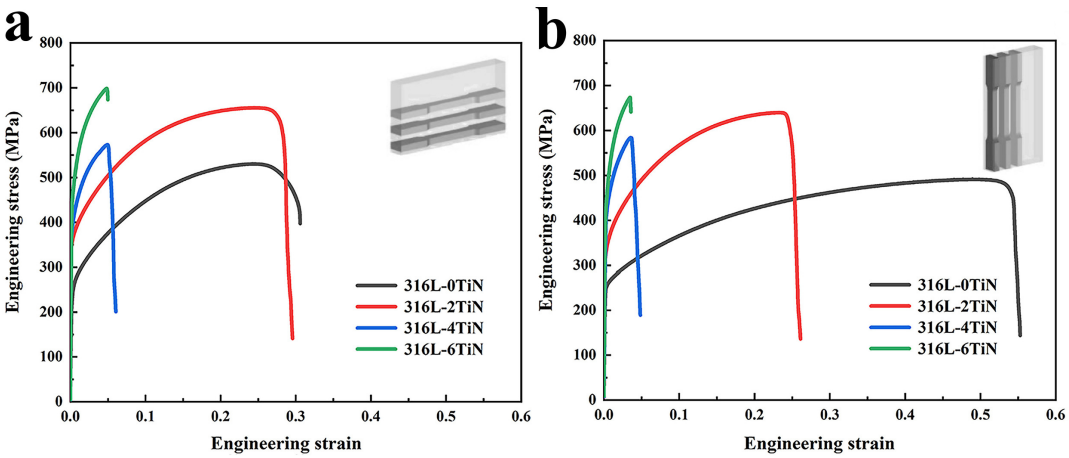

Figure 2.3: Engineering stress–strain curves of all samples with loading axis in the (a) transverse and (b) longitudinal directions. Adapted from Wang et al. [20].

Taken together, these findings highlight the importance of grain refinement and the columnar-to-equiaxed transition (CET), i.e., the transformation of coarse, directional columnar grains into fine-equiaxed grains. These are increasingly recognized as critical pathways for enhancing both the processability and mechanical performance of AM-fabricated components.

This project aims to evaluate the feasibility of achieving grain refinement through in-situ titanium injection during 316L DED, with emphasis on the resulting microstructural modifications and process optimization. The following sections examine the key factors governing stainless steel microstructures and the strategies available for tailored microstructural control.

2.2 Solidification Pathways

The final solidified structure in austenitic stainless steels (A-SS) is determined by the alloy composition, cooling rate, and solute redistribution during solidification. When processed by AM, the γ-austenite phase, with its face-centered cubic (FCC) structure, may form alongside varying fractions of δ-ferrite, which has a body-centered cubic (BCC) structure. Solute rejection at the solidifying interface enriches the intercellular regions with chromium (Cr) and molybdenum (Mo), which results in the formation of ferrite. The ferrite content decreases with increasing cooling rate because of the reduced time for solute redistribution [4]. Table 2.1 summarizes the four principal solidification pathways based on their respective transformation sequences [23].

Mode	Transformation Sequence	Range
Austenitic (A)	$L \rightarrow L + \gamma_{prim.} \rightarrow \gamma$	$(Cr_{eq}/Ni_{eq}) \leq 1.3$
Austenitic–ferritic (AF)	$L \rightarrow L + \gamma_{prim.} \rightarrow L + \gamma + \delta \rightarrow \gamma + \delta$	$1.3 < (Cr_{eq}/Ni_{eq}) \leq 1.5$
Ferritic–austenitic (FA)	$L \rightarrow L + \delta_{prim.} \rightarrow L + \delta + \gamma \rightarrow \gamma + \delta$	$1.5 < (Cr_{eq}/Ni_{eq}) \leq 1.8$
Ferritic (F)	$L \rightarrow L + \delta_{prim.} \rightarrow \delta \rightarrow \delta + \gamma$	$(Cr_{eq}/Ni_{eq}) > 1.8$

Table 2.1: Solidification modes, transformation sequences and Cr_{eq}/Ni_{eq} ranges.

The chromium-to-nickel equivalent ratio (Cr_{eq}/Ni_{eq}) is commonly used to predict the dominant solidification mode. Cr is a ferrite stabilizer, while Ni is an austenite stabilizer. The Cr_{eq}/Ni_{eq} ratio is calculated using the empirical relations [24]:

$$\begin{aligned} Cr_{eq} &= Cr + Mo + 1.5Si + 0.5Nb + 2Ti \ (wt.\%) \\ Ni_{eq} &= Ni + 0.5Mn + 30C + 30N + 0.5Cu + 0.5Co \ (wt.\%) \end{aligned} \tag{2.1}$$

This approach simplifies the multicomponent alloy system with its complex elemental interplay into a pseudo-binary Fe–Cr_{eq}/Ni_{eq} one to assess the propensity for austenite or ferrite formation according to the alloy composition.

Figure 2.4 illustrates the corresponding solidification modes, with the colored lines indicating the Cr_{eq}/Ni_{eq} for the 316L stainless steel powder (1.41 - blue) and substrate (1.44 - red line) based on Eq. 2.1. In the ferritic–austenitic (FA) mode, δ-ferrite nucleates as the primary phase and subsequently transforms into γ-austenite during cooling. Austenite formed via $\delta \rightarrow \gamma$ solid-state transformation typically appears as grain boundary or Widmanstätten austenite. The non-equilibrium conditions of DED, often move solidification towards through single-phase austenitic (A) or ferritic (F) modes. Nonetheless, elemental segregation and local composition can significantly influence

the resulting microstructure [23].

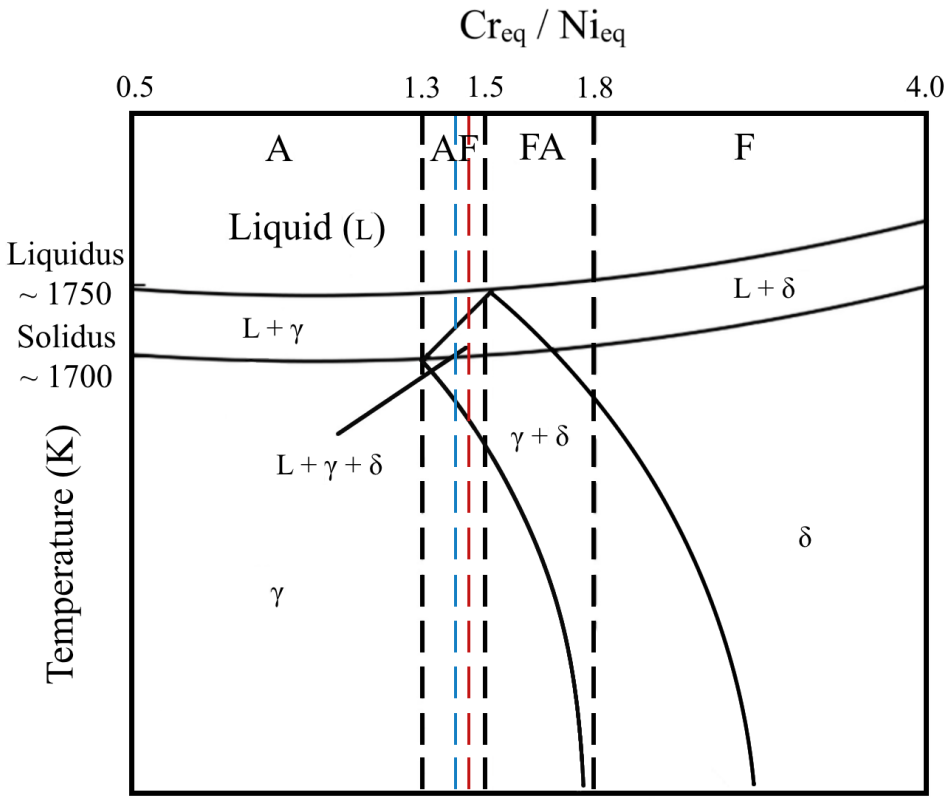

Figure 2.4: Solidification modes of austenitic stainless steels in a pseudo-binary phase diagram, showing the Cr_{eq}/Ni_{eq} ratio for the 316L powder in blue (1.41), and substrate in red (1.44).

2.3 Grain Morphology

As discussed, the solidification regime in metallic systems is governed primarily by alloy composition and cooling rate. It has been widely reported for the DED process that the rapid solidification conditions driven by the steep thermal gradients and high cooling rates typically result in columnar cellular/dendritic and equiaxed microstructures [4, 5, 13, 25, 26]. Columnar grains originate via epitaxial growth from the substrate or previous layers and may span multiple deposition tracks due to their lower nucleation barrier. In FCC austenitic stainless steels, the $\langle 100 \rangle$ growth direction is thermodynamically favored, leading to preferential growth along this axis, a phenomenon referred to as competitive growth [23]. These elongated grains, aligned with the thermal gradient and build direction, induce mechanical anisotropy and increase the risk of hot cracking [4, 21, 27].

Conversely, equiaxed grain formation occurs through two primary mechanisms: (1) constitutional supercooling (ΔT_{CS}) ahead of the solid-liquid (S/L) interface, and (2)

heterogeneous nucleation facilitated by inoculants. As described by the nucleation theories of Winegard and Chalmers [28], the Interdependence theory [29], and the recent numerical nucleation model of Xu et al. [30], successful heterogeneous nucleation and grain refinement require the generation of sufficient undercooling (ΔT) ahead of the S/L interface to exceed the critical nucleation undercooling (ΔT_n) for heterogeneous nucleation; that is, $\Delta T \geq \Delta T_n$. Consequently, ΔT and ΔT_n are two key factors governing grain size and morphology. Fine, equiaxed grains are favored when ΔT is large and ΔT_n is small.

As initially proposed and later confirmed experimentally, ΔT_n is strongly dependent on the lattice misfit or mismatch (δ) between the nucleant particle and the solidifying phase [21, 31]. This relationship is expressed as:

$$\Delta T_n = c_E \, \Delta S_v \, \delta^2 \tag{2.2}$$

where c_E is an elastic constant and ΔS_v is the entropy of phase transition per unit volume [21]. For a particle to act as an effective nucleation site for a grain the δ between the particle and the matrix should be minimized to reduce ΔT_n [21, 22].

For rapidly solidifying alloys, the overall undercooling ΔT, defined as the difference between the melt temperature (T_M) and the alloy liquidus temperature (T_L), can be approximated as the sum of thermal undercooling (ΔT_t) and ΔT_{CS} as later described in Section 2.3.2 [21, 31, 32]. This complex interplay has been encapsulated by the estimated volume fraction of pre-formed equiaxed grains (ϕ), which in its generalized form has been expressed as [26, 32]:

$$\phi = 1 - \exp\left\{ \frac{-4\pi N_0}{3\left[(n+1)\sqrt[n]{K_d \frac{G^n}{R}}\right]^3} \right\} \tag{2.3}$$

Here, N_0 is the number density of active nucleation sites, n is a material-dependent constant (typically $n = 2$), and $K_d = \frac{R}{\Delta T^n}$ is the growth kinetics coefficient, which relates undercooling to growth velocity. When $n = 2$, K_d can be expressed as $K_d = \frac{R}{\Delta T^2}$ [32]. At low values of ϕ, equiaxed grains are readily engulfed by advancing columnar grains through epitaxial growth. As ϕ increases, epitaxial growth is suppressed, promoting the transition to a fully equiaxed structure. The thresholds identified for ϕ show that a columnar morphology is favored when the volume fraction of equiaxed grains is below 0.66%, whereas an equiaxed morphology dominates when this fraction exceeds 49%, meaning that $0.0066 \leq \phi \leq 0.49$ results in a mixed microstructure [33].

2.3.1 Thermal Conditions

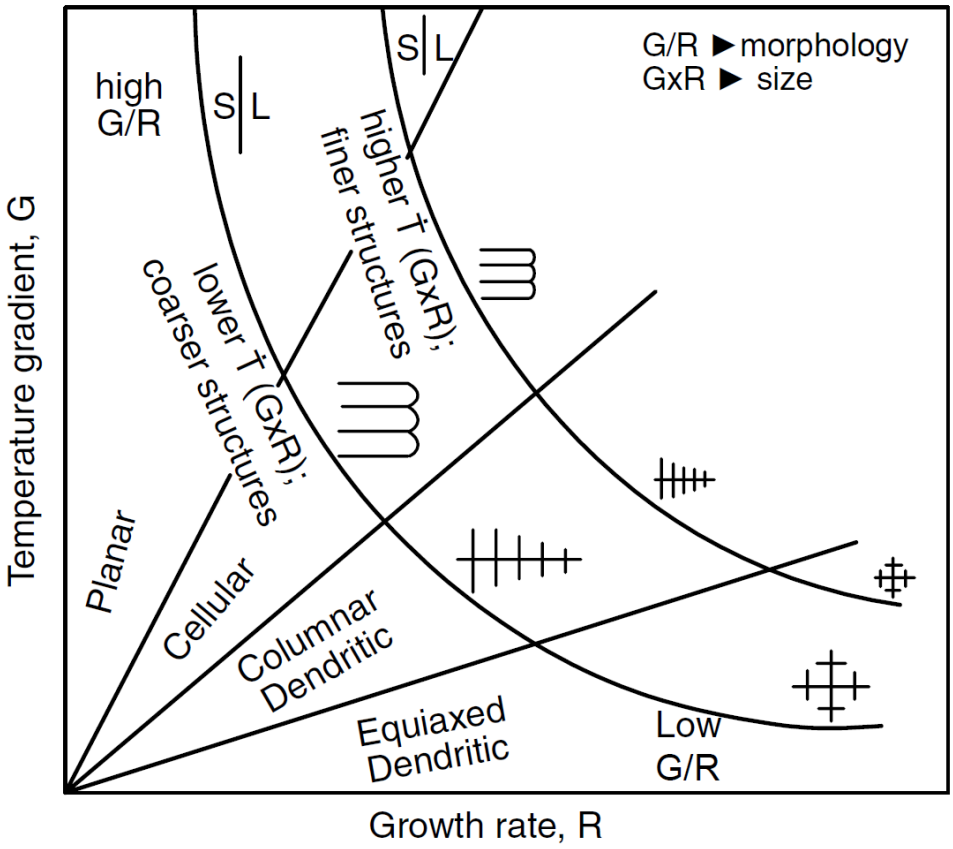

Figure 2.5: Effect of temperature gradient G and solidification/growth rate R on the morphology and size of alloy microstructure. Adapted from Kou [23].

Solidification theory establishes that the morphology of metallic materials, whether columnar, mixed, or equiaxed, is primarily governed by the G/R ratio, while the overall scale of the microstructure is dictated by the cooling rate ($\dot{T} = G \cdot R$), as illustrated in Fig. 2.5 [23]. Combining this with Eq. (2.3) further shows that conditions of low G, high R, small K_d, and large N_0 favor equiaxed grain growth. Alloying elements can influence these parameters by slowing the dendrite growth kinetics, reducing K_d, or by forming stable nucleants. Such nano-precipitates, like nitrides and carbides, increase the number of active nucleation sites N_0, thereby promoting equiaxed solidification. The influence of the solidification rate R on grain morphology can be understood through solute redistribution at the S/L interface, as discussed in the following section.

2.3.2 Solute Redistribution

During solidification, solute elements are rejected into the liquid. At low R, the accumulation of solute atoms rejected from the solid alters the local liquidus temperature,

creating a composition gradient in combination with the thermal field. Borrowing from traditional casting, grain size can therefore be viewed as the outcome of the competition between nucleation and growth, governed by the undercooling ahead of the S/L interface: $\Delta T = \Delta T_t + \Delta T_{\text{CS}}$. A well-established grain refinement strategy for cast and wrought alloys, particularly aluminum, is to manipulate ΔT_{CS} through solutal effects. This concept is formalized in the growth restriction factor (Q), where solute elements with high Q values decrease the latent heat release, allowing for a larger undercooling, thus lowering the effective energy barrier for heterogeneous nucleation to occur [28, 29, 32]. Neglecting diffusion effects, the efficiency of a solute in generating ΔT_{CS} and increasing Q is expressed as:

$$Q = \sum_i m_i C_{0i}(1 - k_i) \text{ (K)} \tag{2.4}$$

where m_i is the slope of the liquidus line, C_{0i} is the concentration of solute i, and k_i is the partition coefficient between solid and liquid solute concentrations $(k_i = \frac{C_{si}}{C_{li}})$ [32]. A larger Q corresponds to stronger solute rejection, greater ΔT_{CS} at the S/L interface, favoring nucleation and thus more effective grain refinement with grain size and showing a linear relation to the reciprocal of the growth restriction factor $(\propto 1/Q)$ [14, 29, 32]. Given Eq. (2.4), the solute selected as the refining element should have a low partition coefficient (k < 1), a steep m, and be strongly rejected into the liquid. In summary, the selected refining element should ideally fulfill the following criteria [34]:

1. Low solute solubility,
2. Readiness to partition into the liquid,
3. Solubility and the eutectic composition should be away from each other to achieve a small k value.

Given these characteristics, a eutectic reaction is a sign that the solute has the right thermodynamic behavior (low k, steep m) to maximize Q and thus refine grains effectively [14].

Solute redistribution also affects thermal undercooling (ΔT_t), which arises from a lag between the actual R of the S/L interface and the theoretical growth rate imposed by the cooling rate $(\dot{T})$ in the melt [32]. Factors such as increased viscosity, reduced atomic mobility, and nucleation density slow the advance of the S/L interface, leaving liquid ahead of the front supercooled below its equilibrium freezing point. Thus, ΔT_t is governed by $\dot{T}$, and solute rejection, since solutes with low solubility and slow diffusivity delay dendrite growth, thereby enhancing ΔT_t [32].

2.4 Grain Refinement Strategies

This section aims to contextualize the various possible refinement strategies with respect to the selected process and material, and clarifies the reason for the injection approach selected for this study. Based on the above mechanisms and Eq.s (2.2),(2.3), and (2.4), several strategies could be implemented to promote grain refinement in AM-fabricated A-SS:

- Altering the solidification mode,
- Reducing the G/R ratio,
- Increasing the growth restriction factor (Q),
- Enhancing the density of nucleation sites (N_0) via inoculants with low critical nucleation undercooling (ΔT_n).

Refinement via a shift in the solidification mode, while feasible, is not ideal. As shown in Eq. (2.1) and the binary equilibrium phase diagram, titanium acts as a strong ferrite stabilizer. This is due to titanium's tendency to form carbide and nitride compounds, which reduces the effective carbon and nitrogen content in the steel and promotes the formation of a ferritic microstructure. These effects are reflected in the Cr_{eq}/Ni_{eq} as calculated in Eq. (2.1). An increase in the ferrite fraction in 316L generally reduces corrosion resistance, especially in high-temperature oxidizing media [15]. It can also decrease low-temperature impact strength and transform into a brittle sigma phase at elevated temperatures, affecting weldability and overall mechanical properties [4, 23]. In DED, the inherently high thermal gradients $(G \sim 10^4\text{–}10^7\,\text{K/m})$ and solidification rates $(R \sim 10^{-4}\text{–}10^{-1}\,\text{m/s})$ make suppression of columnar growth by reducing the G/R ratio particularly challenging [4, 19]. These solidification conditions also limit the effectiveness of solute-based grain refinement. The rapid cooling rates characteristic of AM restrict solute diffusion, leading to solute trapping in the solid phase. Under such conditions, the partition coefficient approaches unity $(k \approx 1)$, which reduces Q as seen in Eq. (2.4). Consequently, achieving solute-driven refinement in AM often requires relatively large alloying additions, which may promote the formation of undesirable phases. For example, CET in Al alloys has been reported to require ∼9 wt.% Cu in Al or ∼4 wt.% Si in 7075 Al [34]. At very high cooling rates $(\dot{T})$, solute seems to play a slightly different role. The actual growth of the dendrites substantially lags the theoretical S/L front velocity R, leading to a difference between the actual dendrite tip temperature and its thermal equilibrium, generating ΔT_t. This undercooled zone can contribute to nucleation events [14, 29, 31, 35]. Zhai [14] has shown that in-situ alloying of 316L with Ti during L-PBF can produce grain refinement from 16.7 to 0.8 µm, without introducing undesirable intermetallic phases.

Alloy	316L-0.3Ti	316L-1Ti	316L-1.5Ti	316L-3Ti
Q (K)	2	6.7	10	20

Table 2.2: Ti contents (wt.%) and the corresponding Q values [14].

Samples fabricated with varying Ti wt.%, as reported in Table 2.2, showed grain sizes directly proportional to $(1/Q)$ as shown in Fig. 2.6. EDS of the precipitates in the alloyed specimens suggested that Ti addition in 316L predominantly leads to TiO_2 formation, which is not an effective inoculant due to its large ΔT_n. The researchers attributed the observed grain refinement mainly to the solute effects of Ti. However, other studies suggest that the role of solute and the Q based approach cannot be directly translated from casting to AM processes [34]. The low Ti content and steep thermal gradients typical of AM bring non-equilibrium conditions limiting the actual increase of Q and subsequent ΔT_{CS}. Therefore, solute-based mechanisms cannot be the sole explanation for the observed microstructural transitions.

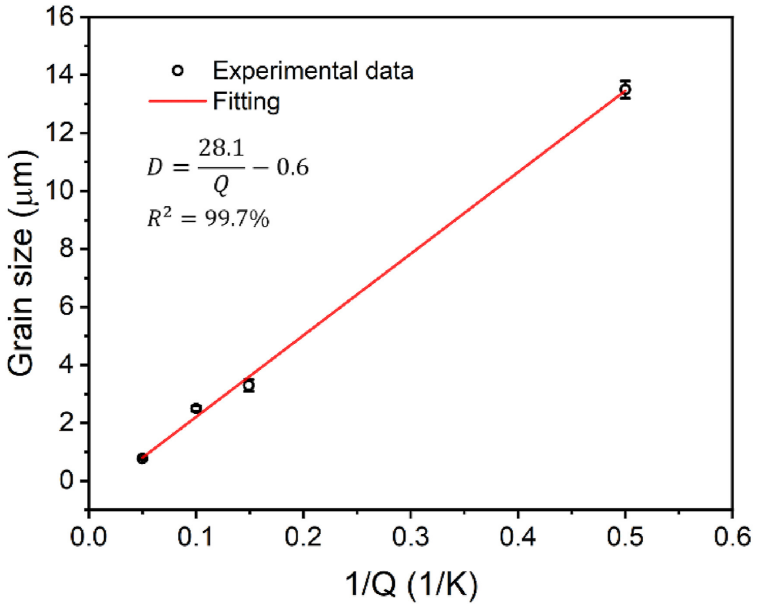

Figure 2.6: Linear relation between grain size of Ti-modified 316L and the reciprocal of growth restriction factor $1/Q$ [14].

Titanium was selected in this study to evaluate its grain-refining potential in 316L, with the primary hypothesis that Ti injection during DED can promote the in-situ formation of established refining particles such as TiN and TiC. In addition, titanium can form a eutectic with iron: in the Fe–Ti system, a eutectic reaction occurs near 14 wt.% Ti, producing brittle Laves phases (Fe_2(Ti,Nb)) (Fig. 2.7). While these characteristics may reduce the nucleation barrier and favor the CTE transition by increasing Q (Section 2.3.2), the resulting Laves phase compromises mechanical integrity due to its brittleness. Moreover, excess titanium acts as a strong ferrite stabilizer, increasing the ferrite volume

fraction, which is also undesirable in 316L. The objective of this project was therefore to introduce just enough Ti to trigger grain refinement via in-situ TiN and TiC precipitation, while keeping the Ti content low enough to avoid fully ferritic structures or Laves phase formation. Consequently, manipulating Q through heavy alloying additions was not considered a viable strategy for grain refinement in DED-processed 316L.

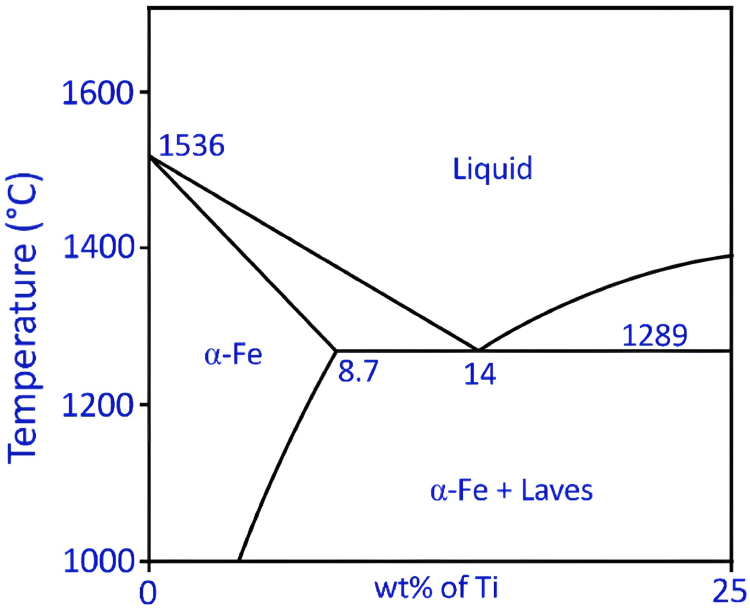

Figure 2.7: Binary phase diagram of Fe–Ti [14].

In contrast, inoculation is a more robust and widely validated approach. As discussed, effective inoculants are characterized by a low lattice mismatch and interfacial energy with the matrix, which reduces the undercooling threshold for heterogeneous nucleation ΔT_n. This method has been successfully translated to AM processes: Tan et al. [36] demonstrated significant austenite grain refinement in L-PBF tool steel using 0.5 wt.% TiN nanoparticles. Similarly, Mo [37] reported grain refinement in laser-clad 420 stainless steel with up to 6 wt.% TiC andWang et al. [18] observed comparable results in DED 316L stainless steel with up to 2-4 wt.% TiN.

Figure 2.8(a–d) shows IPF maps obtained by EBSD for L-PBF fabricated 316L stainless steels with varying TiN nanoparticle additions (0.5, 1, and 2 wt.%), as reported by Tan et al. [21]. All IPF maps are aligned along the build direction, with the color scale representing grain orientations. Ultrasonic-assisted vibrational agitation was employed for powder mixing. The corresponding pole figures (Fig. 2.8(e–h)) illustrate the effect of TiN addition on crystallographic texture, where the color scale indicates the relative intensity of the diffraction peaks. The shift in grain size distributions with TIN addition is summarized in Fig. 2.8(i).

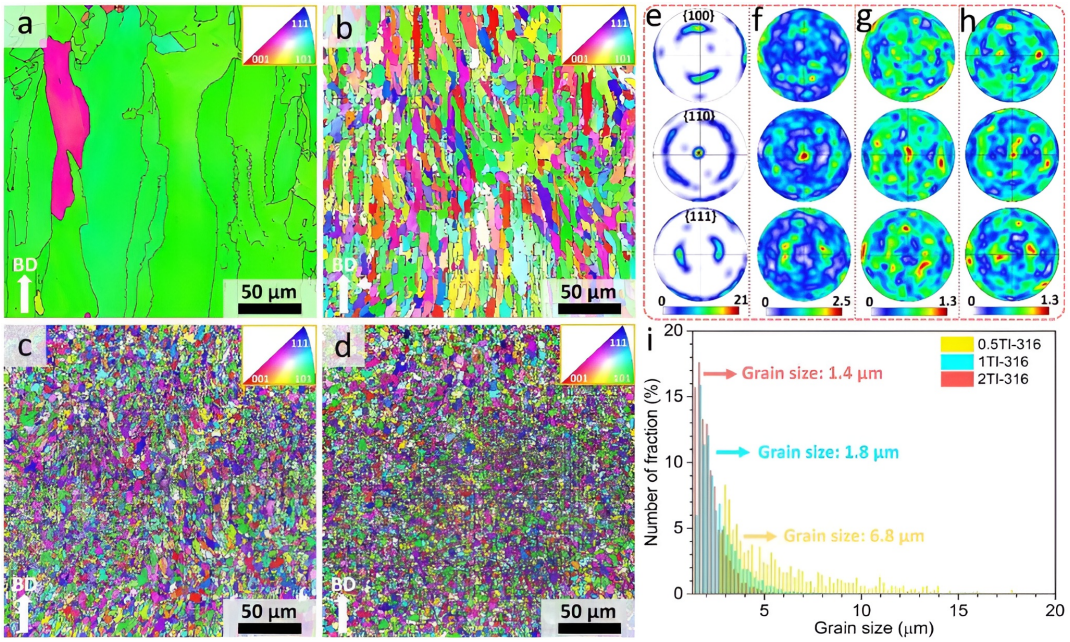

Figure 2.8: Longitudinal EBSD-IPF grain orientation maps (a–d) and corresponding pole figures (e–h) of L-PBF fabricated 316 steel with varying TiN nanoparticle additions (0.5, 1, and 2 wt.%): (a, e) 316 steel, (b, f) 0.5TiN–316 steel, (c, g) 1TiN–316 steel, (d, h) 2TiN–316 steel. (i) Grain size distribution of the TiN–316 steels [21].

The results show that the addition of TiN nanoparticles transformed the microstructure from coarse columnar grains with a strong $\langle 110 \rangle$ texture (Fig. 2.8(a,e)) into fine, equiaxed grains with random orientations (Fig. 2.8(b–d,f–h)). This refinement was attributed to TiN nanoparticles acting as potent heterogeneous nucleation sites, suppressing epitaxial growth and promoting equiaxed grain formation.

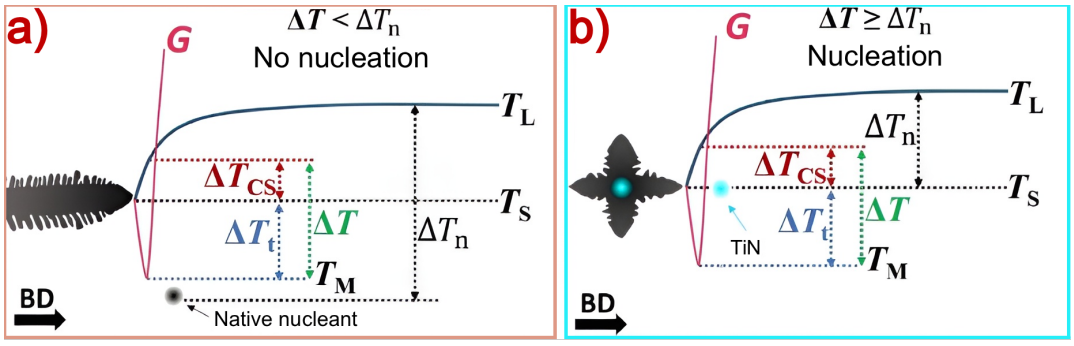

Figure 2.9: Schematic illustration of undercooling generation ahead of the S/L interface and the critical nucleation undercooling (ΔT_n): (a) 316L stainless steel without TiN and (b) TiN-modified 316L. Here, G denotes the thermal gradient, and T_S, T_L, and T_M represent the solidus, liquidus, and melt temperatures, respectively. Adapted from Tan et al. [21].

The mechanism is consistent with the Interdependence Theory and is illustrated in Fig.

2.9. In unmodified 316L (Fig. 2.9(a), columnar grains grow epitaxially under high thermal gradients G. The native oxides present have a high ΔT_n and do not meet sufficient ΔT to stimulate nucleation ahead of the S/L interface. In contrast, in TiN-modified 316L (Fig. 2.9(b), the nanoparticles lower the ΔT_n barrier, and, together with solutal effects, promote heterogeneous nucleation, enabling the transition to equiaxed grains.
Durga et al. [27] similarly reported the in-situ formation of TiO_x core–TiN shell particles during the L-PBF fabrication of an AISI 441 ferritic steel with 1 wt.% Ti addition, where TiN acted as the effective inoculant (Fig. 2.10).

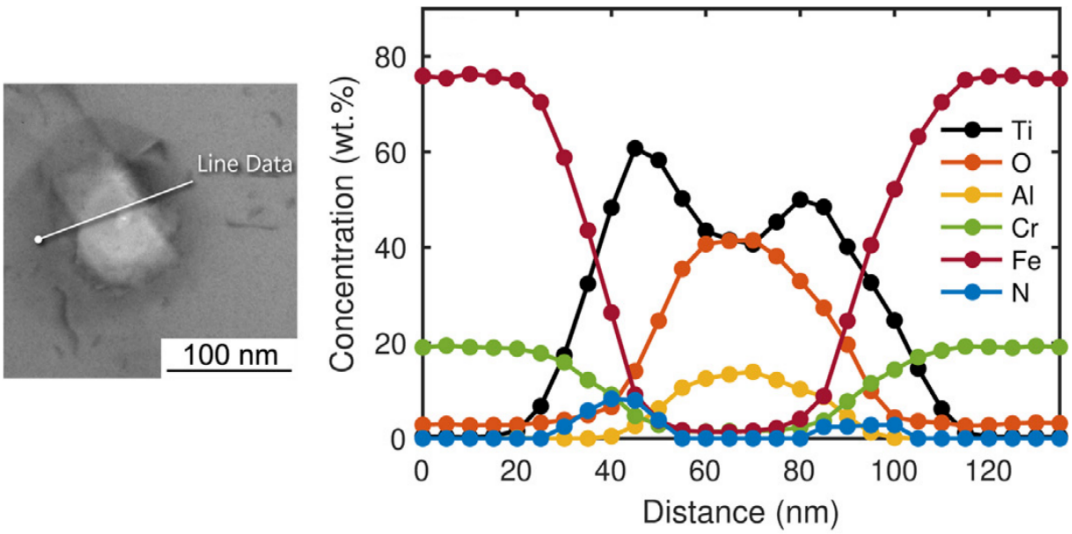

Figure 2.10: STEM-EDS line scan of an irregularly shaped particle found in the equiaxed zone of Ti-enriched AISI 441 ferritic steel [27].

Despite these advances, the precise mechanisms responsible for grain refinement remain under debate. The present study adopts a similar principle, using in-situ tailoring to refine the microstructure of 316L, but applies it in the context of DED. The following section details the process design and the rationale for selecting titanium powder as the refining agent to inject.

2.4.1 In-situ Refinement

In-situ grain refinement involves introducing refining agents during the build process, thereby enabling dynamic control over the evolving microstructure. Building on previous studies, this project investigates the feasibility of tailoring the microstructure of 316L stainless steel in DED through titanium injection to promote the in-situ formation of grain-refining nano-precipitates such as TiN and TiC. Commercially pure Ti particles were selected because direct injection of preformed TiN or TiC nanoparticles is impractical in DED. The high thermal stability of TiN and TiC can limit their dissolution and interaction with the matrix [21]. Furthermore, nanoparticles often fail to penetrate the

melt pool due to dominant surface forces, while larger particles are generally less effective refiners as micron-scale particles present a lower surface area per unit volume compared to nanoparticles. The reduced surface area provides fewer potential nucleation sites, reducing N_0 for new grains during solidification.

To calculate the minimum particle size required to penetrate the melt pool, one can analyze the dynamics of the particle impact on the melt. The incorporation of a solid spherical particle of radius r (m) and density ρ_s (kg/m^3) impacting with normal velocity v (m/s) into a liquid of density ρ_l (kg/m^3) and surface tension σ (J/m^2) is governed by the Weber number (We), a dimensionless parameter expressing the ratio of a particle's kinetic energy to its surface energy [38]:

$$\mathrm{We} = \frac{r\rho_l v^2}{\sigma} \tag{2.5}$$

A critical Weber number, $\mathrm{We}_{\mathrm{cr}}$, defines the threshold above which $(\mathrm{We} > \mathrm{We}_{\mathrm{cr}})$ particle penetration into the melt pool occurs, while below it $(\mathrm{We} < \mathrm{We}_{\mathrm{cr}})$, particles are entrapped at the surface:

$$\mathrm{We}_{\mathrm{cr}} \approx \frac{6(1-\cos\Theta)}{\rho^* - 0.222} \tag{2.6}$$

Here, $\rho^* = \rho_s/\rho_l$ is the dimensionless density ratio. This expression, derived from theoretical and experimental models, assumes equilibrium at $v = 0$, where only fully wetted particles with zero contact angle $(\Theta = 0^\circ)$ can be incorporated into the melt pool [38]. Equation (2.6) neglects gravity, making it valid for particles smaller than 0.1 mm in radius. Smaller particles could be forced into the melt by accelerating them to higher speeds, though in practice, particle velocity v is limited by the carrying gas velocity u, which itself must remain below the critical threshold to prevent melt pool splashing. The critical velocity u_{cr} can be estimated using the Kelvin–Helmholtz instability criterion [39]:

$$u_{\mathrm{cr}}^2 \approx 2\frac{\sqrt{g\rho_l\sigma}}{\rho_g} \tag{2.7}$$

Using $\sigma = 1.8$ J/m^2, $\rho_l = 8000$ kg/m^3, and $\rho_g = 0.96$ kg/m^3 (estimated via the ideal gas law for Ar at 500 K and 1 bar), the critical gas velocity is calculated as $u_{\mathrm{cr}} = 28$ m/s. By combining the successful incorporation condition $(\mathrm{We} > \mathrm{We}_{\mathrm{cr}})$ with $v \le u \le u_{\mathrm{cr}}$, a critical particle radius r_{cr} can be derived:

$$r_{\mathrm{cr}} = \frac{3(1-\cos\Theta)}{\rho^* - 0.222} \cdot \frac{\rho_g}{\rho_l} \cdot \sqrt{\frac{\sigma}{g\rho_l}}\ (\mathrm{m}) \tag{2.8}$$

Therefore, only particles with $r > r_{\mathrm{cr}}$ can be entrained by the gas stream and penetrate the melt pool without inducing surface instabilities [39].

Table 2.3 summarizes the calculated critical particle sizes for common grain refining agents, including both unoxidized and oxidized forms, assuming the extreme case of maximum gas velocity ($v = u_{\mathrm{cr}}$ from Eq. (2.8)) and a standard condition for the DED setup used in the study of $v = 7$ m/s [40]. These results demonstrate that TiN and TiC nanoparticles have a lower probability of entering the melt pool, as even with the fastest gas flow possible, the r_{cr} would range from 1.36-5.11 µm and 0.52-7.25 µm. These micrometer-sized dimensions are several orders of magnitude larger than the nanometer scale.

Particle	ρ_s (g/cm^3)	ρ^*	Θ (°)	$\mathrm{We}_{\mathrm{cr}}$	r_{cr} (µm) $v = 28$ m/s	r_{cr} (µm) $v = 7$ m/s
TiC	4900	0.613	28	1.80	0.517	8.26
TiC (oxid.)	4900	0.613	130	25.2	7.25	116
TiN	5400	0.675	50	4.73	1.36	21.7
TiN (oxid.)	5400	0.675	110	17.8	5.11	81.6
Ti	4510	0.564	0	0	0	0
Ti (oxid.)	4510	0.564	90	17.6	5.04	80.6

Table 2.3: Density of the solid, density ratio, contact angle, Critical Weber numbers and critical particle sizes for various steel-refining particles in both oxidized and unoxidized forms [38, 41].

Larger TiN and TiC particles could be considered, but their size and high temperature stability could prevent them from diluting into and interacting with the surrounding matrix. TiN and TiC are stable compounds with high melting points (TiN 2950°C, TiC 3160°C), much higher than Ti (1668°C). During DED, the high temperatures may not be sufficient to fully dissolve these larger particles into the 316L matrix, especially if the dwell time is short. Of the particles analyzed, commercially pure titanium particles appear viable for melt pool penetration under typical DED conditions. Their relatively better wettability allows incorporation without requiring extreme particle size or velocity.

Moreover, titanium injection is not expected to present dissolution issues, as the steep thermal gradients at the liquid steel surface induce strong Marangoni convection [39, 42, 43, 44]. This phenomenon drives the liquid from low to high surface tension regions as a function of the temperature coefficient of the surface tension ($\frac{d\sigma}{dT}$), resulting in material fluxes flowing from high-temperature to low-temperature regions on the melt pool surface, resulting in the Marangoni convection shown in Fig. 2.11. Section 4.2 provides a more detailed look into the relation between $\frac{d\sigma}{dT}$ and the Marangoni convection flow patterns.

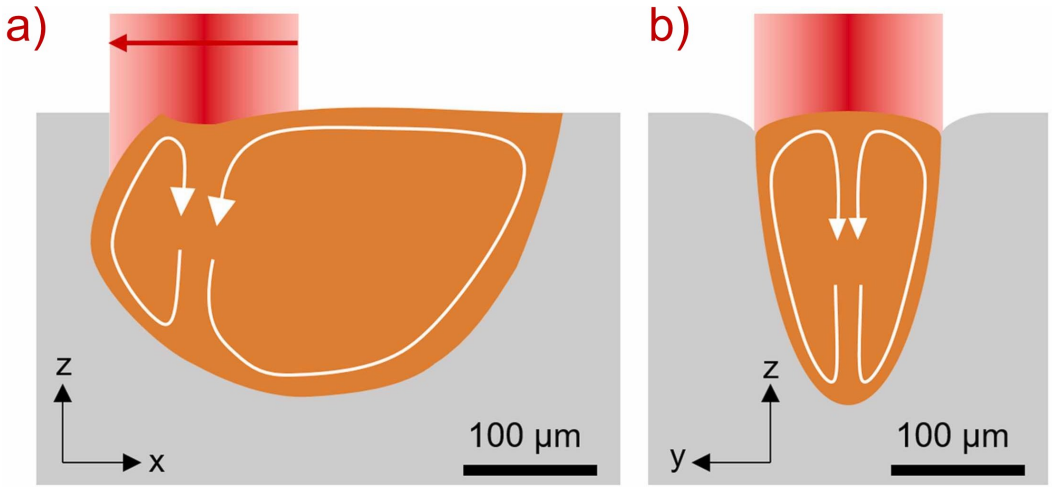

Figure 2.11: a) Side view of melt flow pattern in the center plane (y = 0); b) Front view of melt flow pattern. **NOTE:** Schematics adapted from Yang et al. [42].

Unlike premixed powders, which suffer from segregation due to density and morphological differences, in-situ Ti injection enables more uniform dispersion and could offer real-time, multi-axial compositional control for microstructure modification. This novel aspect of this work is fostered by the hypothesis that DED processing can facilitate the in-situ formation of titanium-rich grain refiners, such as TiC and TiN, and oxynitride (Ti–O–N) compounds. Since nitrogen and carbon are inherently present in steel and titanium readily forms stable oxides, these oxides can act as precursors or catalysts for subsequent precipitates. The potential for Ti-rich formations for grain refinement is further supported by the literature reviewed and the established role of TiN and TiC as potent inoculants in the casting and welding of stainless steels, where it is used to trigger heterogeneous nucleation [20, 21, 22, 27].

Chapter 3

Materials and methods

3.1 Substrate Material

The substrate for deposition consisted of 316L stainless steel plates with dimensions of 50×100 mm^2 and a thickness of 4 mm. The plates were sandblasted to roughen their surface and minimize laser back reflection. The supplier (HABA AG, Cham, Switzerland) provided the chemical composition listed in Table 3.1.

Element	Cr	Ni	Mo	Mn	Si	N	C	P	S	Fe
wt.%	18.5–16.5	13.0–10.0	2.50–2.00	≤ 2.00	≤ 1.00	≤ 0.11	≤ 0.03	≤ 0.045	≤ 0.015	Balance

Table 3.1: Chemical composition of the 316L stainless steel substrate.

3.2 Powder Feedstocks

The 316L stainless steel feedstock was Gas Atomised CT PowderRange 316LE Rev2 (Carpenter Additive®), with a particle size range of 45–106 µm measured via the Morphologi 4 from Malvern Panalytical as shown in the red line in Fig. 3.1. Its certified composition is shown in Table 3.2.

Element	Cr	Ni	Mo	Mn	Si	N	C	P	S	Fe
wt.%	17.8	12.7	2.44	0.91	0.56	0.09	0.025	0.009	0.011	Balance

Table 3.2: Chemical composition of the 316L powder feedstock (45–106 µm).

The titanium feedstock was commercially pure Ti grade 1 powder (AP&C Advanced Powders & Coatings Inc., Quebec, Canada), with a particle size range of 45–106 µm and a composition compliant with ASTM B348 [45], listed in Table 3.3.

Element	O	C	N	H	Fe	Other each	Other total	Ti
wt.%	≤ 0.08	≤ 0.02	≤ 0.02	≤ 0.002	≤ 0.03	≤ 0.1	≤ 0.4	Balance

Table 3.3: Chemical composition of cp-Ti grade 1 powder (45–106 µm) [46].

The particle size distribution, measured by laser diffraction per ASTM B822, is shown in

Fig. 3.1 as the green line [46]. Powder morphology was highly spherical with minimal satellites or voids, as shown exemplarily by SEM imaging for cp-Ti (Fig. 3.2).

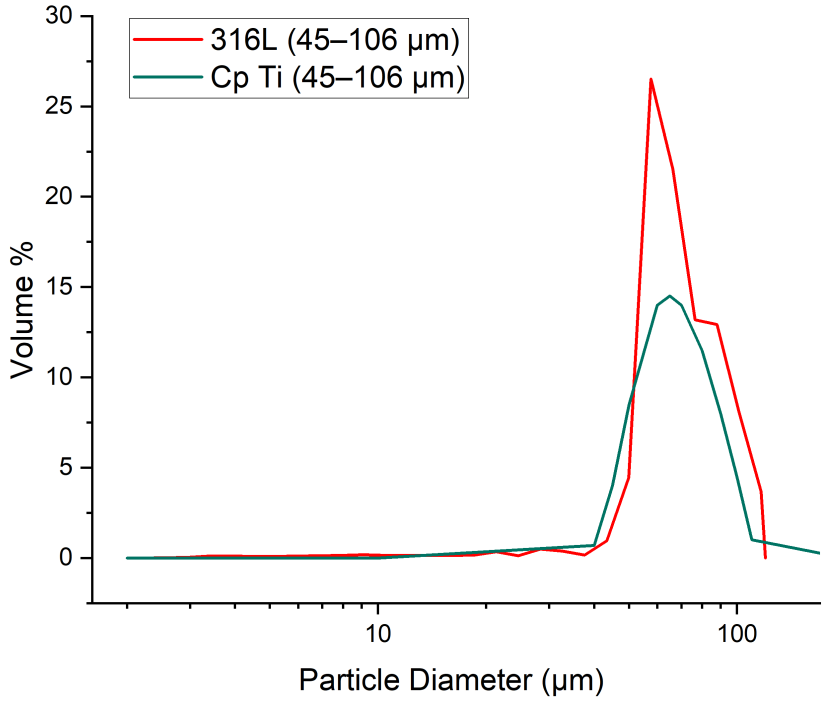

Figure 3.1: Particle size distribution of Cp-Ti powder (green) measured by laser diffraction [46] and 316L powder (red).

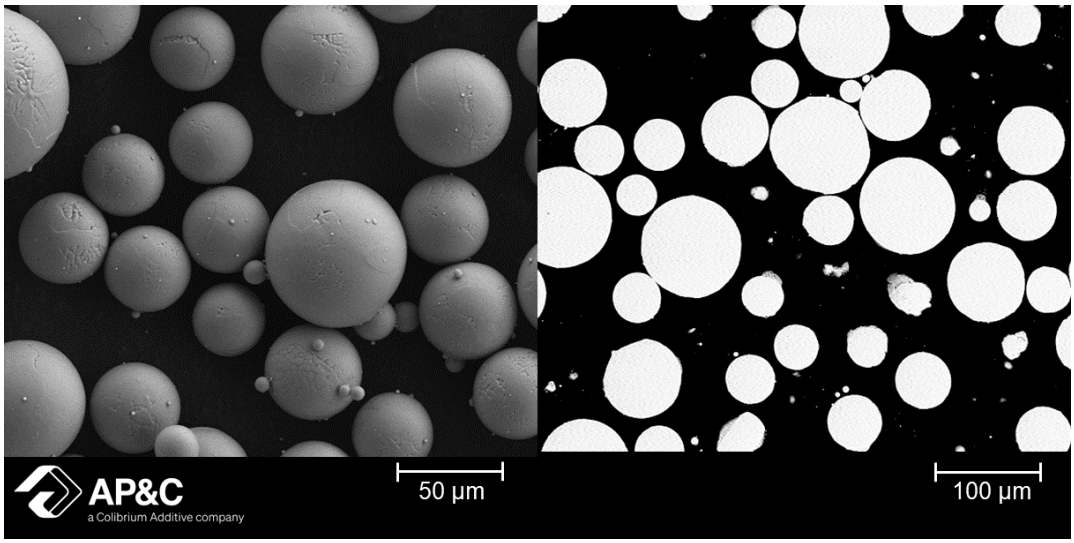

Figure 3.2: SEM images of Cp-Ti powder particles and metallographic cross-sections [46].

3.3 Directed Energy Deposition System

Experiments were performed on a BeAM Mobile 1.0 DED machine (BeAM Machines by AddUp, Cébazat, France), equipped with a 3-axis arm for nozzle positioning and a 2-axis substrate platform. The maximum nozzle speed is 30,000 mm/min. The processing chamber and reference axes are shown in Fig. 3.3.

Figure 3.3: BeAM Mobile 1.0 DED machine chamber with reference axes.

3.3.1 Laser Beam Specifications

The system uses a continuous-wave Yb-fiber laser (YLR-Series, IPG Photonics, Oxford, MA, USA) operating at 1068 nm with a maximum power of 500 W. The beam has a Gaussian profile, a focal spot of 800 µm, and Rayleigh length of 18 mm. All samples were printed at a constant laser power of 300 W.

3.3.2 Nozzle Head

The coaxial nozzle (Fig. 3.4) consists of three copper cones forming one central and two annular channels. Copper provides high thermal conductivity and is water-cooled to prevent overheating. The central channel delivers the laser beam and primary shielding gas (3 L/min). The intermediate channel supplies the shaping gas (6 L/min). The outer channel conveys powder entrained in the shield gas. The combined gas flow focuses the powder into a 1 mm spot approximately 3.5 mm below the nozzle exit, aligning the powder and laser foci at the substrate surface.

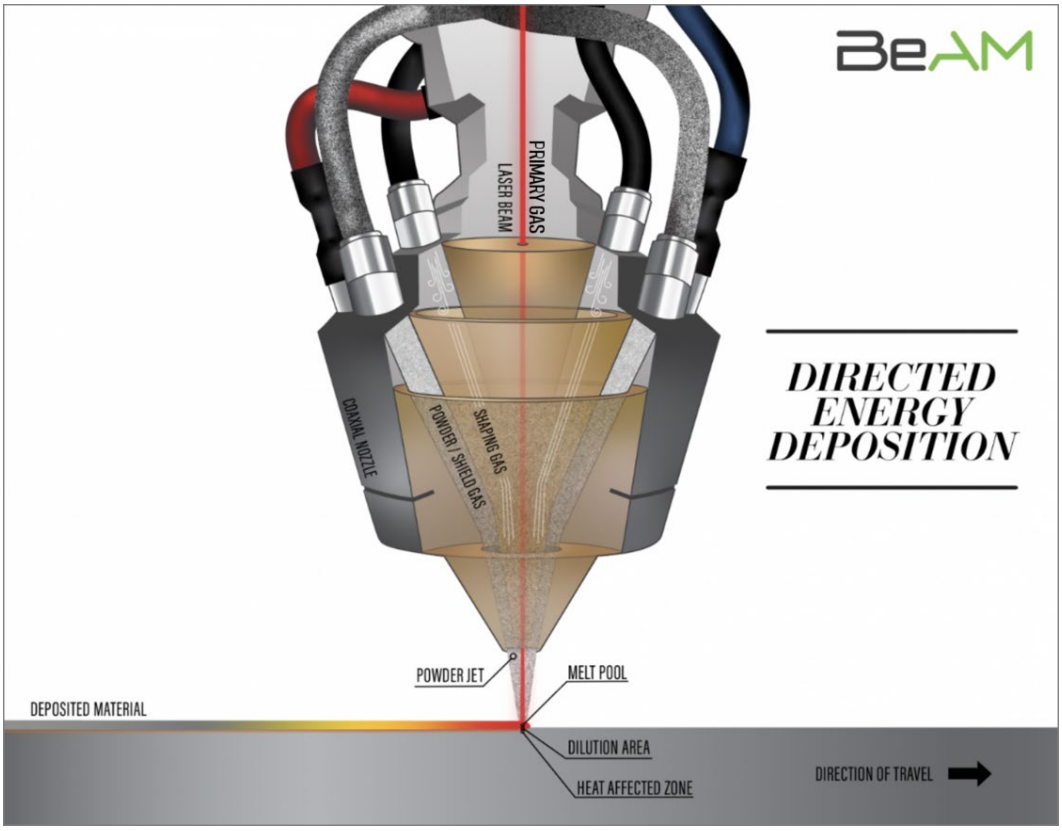

Figure 3.4: Schematic of the coaxial DED nozzle head.

3.3.3 Powder Feeding System

Two volumetric powder feeders (Medicoat AG, Switzerland) supplied 316L and Ti powders (Fig. 3.5). Powder in each reservoir is agitated onto a rotating plate (turn-plate), where a fixed baffle redirects it into the carrier gas stream. Argon gas entrains the powder to the nozzle. Continuous feeding was later found to require a turn-plate speed of 6% of maximum (0.6 RPM) as lower speed would result in jitter of the turn plate and inconsistent feed rate.

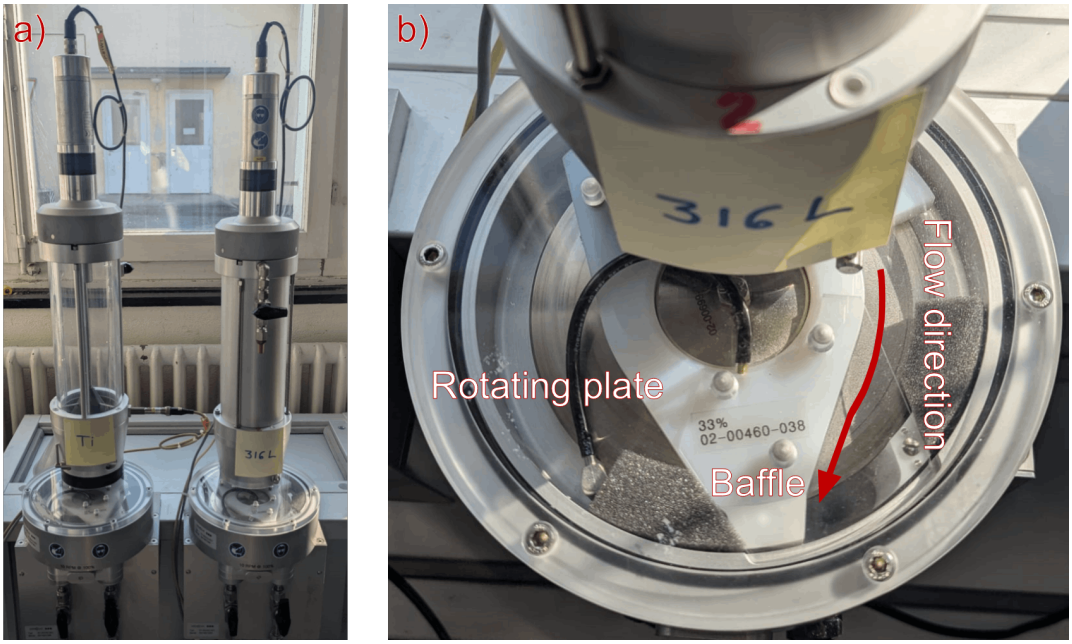

Figure 3.5: a) Volumetric powder feeders; b) rotating plate mechanism.

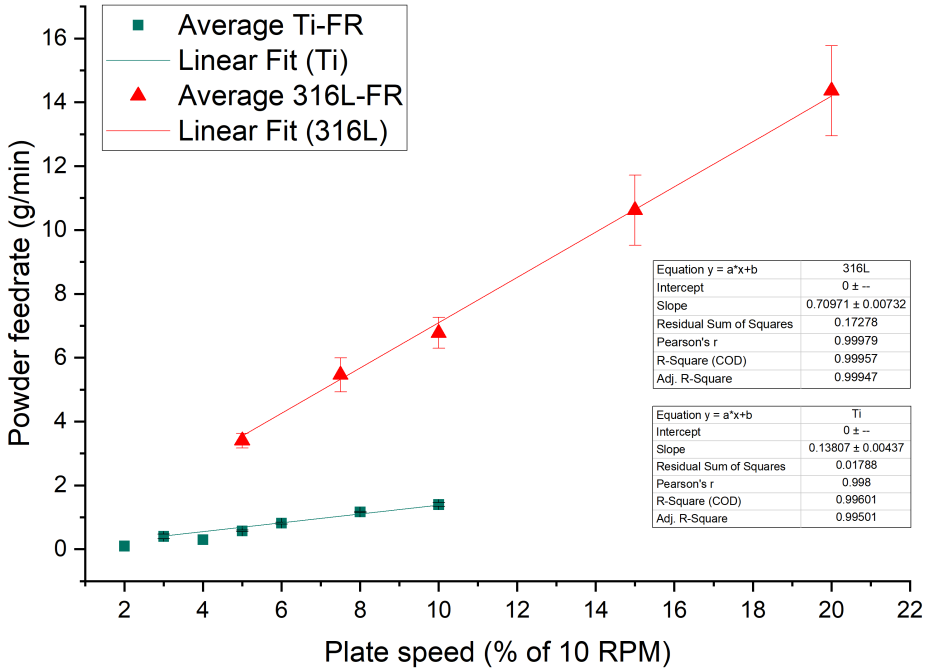

Figure 3.6: Measured powder feed rates for 316L (red) and Ti (green) as a function of rotating plate speed.

The measured Ti and 316L feed rates as a function of plate speed are shown in Fig. 3.6. As mentioned, plate speeds below 0.6 RPM resulted in non-constant feed rate.

3.4 Sample Fabrication

3.4.1 Preliminary Tests

The preliminary tests aimed to investigate the effect of in-situ Ti injection on the solidification microstructure of 316L stainless steel plates during L-DED. Single 2 mm long track were fabricated with varying Ti feed rates (0, 0.4, and 0.6 g/min) and nozzle velocities (NV) of 1500, 2000, 2500, and 5000 mm/min. Figure 3.7 shows the preliminary single tracks as printed on the sandblasted 316L substrate.

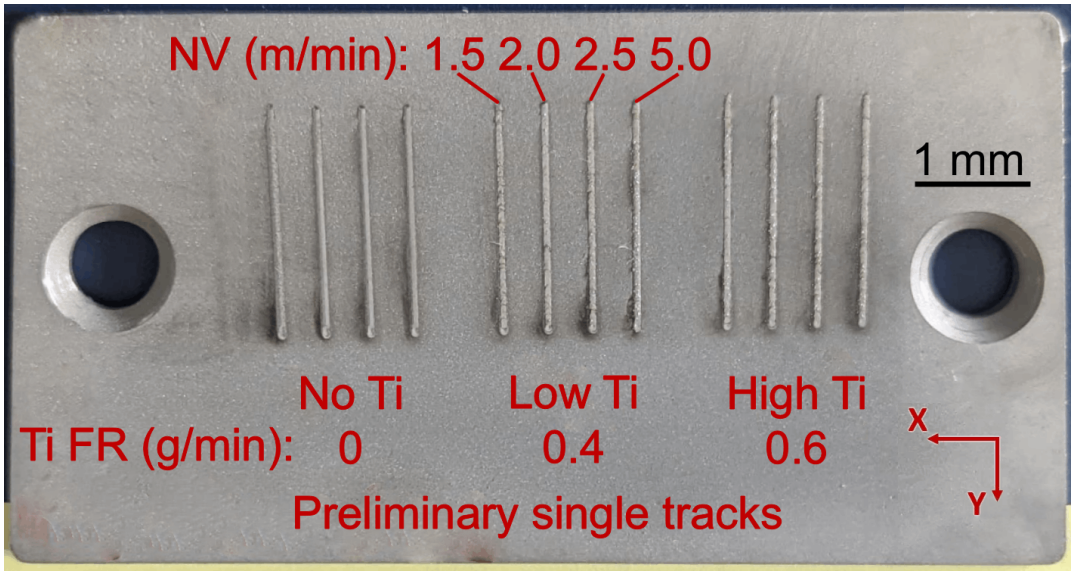

Figure 3.7: Preliminary single-track samples deposited with varying Ti feed rates (Ti FR) and nozzle velocities (NV), with machine reference axes indicated.

Additionally, bulk "sandwich" structures with base 10×10 mm^2 were fabricated by alternating several millimeters of 316L (NV = 1000 mm/min and 316L FR = 5.0 g/min) with two Ti layers deposited at Ti FR = 0.4 g/min and varying speeds. The high NV did not produce layers consisting of pure Ti but rather Ti enriched layers as the low feed rate and high nozzle speed led to rescanning of the underlying 316L in which Ti was diluted. This simple and repeatable structure was selected to provide information on the repeated deposition of Ti and further demonstrate the possibility to locally tailor the material's microstructure.

Figure 3.8(a) shows a representative sandwich sample after etching where the Ti layers are clearly visible. The layer height was 0.2 mm with hatch spacing of 0.5 mm. The scanning strategy was bi-directional with a 90° rotation between subsequent layers as shown in Fig. 3.8(b). Laser scanning strategies can affect the temperature gradient G, resulting in samples with more unmelted powder, pores, and cracks under the 0° scanning strategy than those under the 90° scanning strategy when processing 316L

through DED [47]. Moreover, this scanning pattern was selected to minimize the distortion effects of the moving heat source on the grain growth and to avoid producing the same orientation of G over several layers.

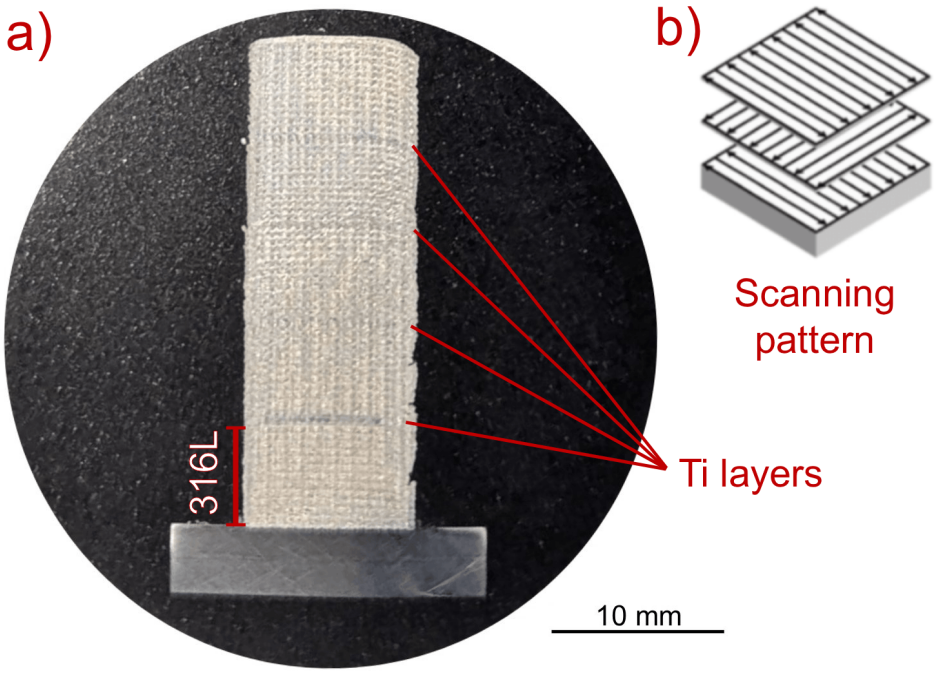

Figure 3.8: a) Representative bulk "sandwich" sample alternating 316L layers with two pure Ti layers at high injection speeds; b) Bi-directional scanning pattern with 90° rotation between subsequent layers.

These preliminary trials established the baseline process behavior for Ti injection, highlighting track stability, dilution of Ti in the melt pool, and potential for grain refinement.

3.4.2 Model, Toolpath, and Code

Toolpaths for single tracks and bulk samples were generated by specifying nozzle velocity, hatch spacing, and layer height. A representative G-code snippet for bi-directional bulk deposition is provided in Appendix B (Code 1).

3.4.3 Parametric Study Design

Based on the preliminary test results, an experimental campaign was designed to evaluate the effects of process parameters on solidification behavior, grain refinement, and phase evolution. Single-track deposits with Ti injection on 316L substrates were selected to isolate process–structure relations. The key process variables were:

- **Nozzle Velocity (NV):** 1000 to 10,000 mm/min in 1,000 mm/min increments Controls heat input and melt pool dimensions.

- **Ti Feed Rate (Ti FR):** 0, 0.9, and 1.2 g/min
  Alters local composition and heterogeneous nucleation potential.
- **Number of Rescanning Passes (R):** 0 (as-deposited) and 1 (single rescan with no Ti injection)
  Evaluates the influence of thermal cycling and melt pool mixing.

This parametric study was structured to investigate the combined effects of NV, Ti FR, and R on solidification morphology (columnar versus equiaxed) as well as ferrite stabilization in austenitic 316L, grain refinement and microstructural homogeneity. It is important to note that the feed rate values shown in Fig. 3.6 are specific to the setup used in this study. The described transitions and phenomena should therefore be interpreted relative to the actual amount of titanium introduced. However, since precise Ti wt.% quantification required EDS scans, the majority of the trends are reported in terms of the indirect process parameters of nozzle velocity (NV) and titanium injection feed rate (Ti FR).

3.5 Microstructure Characterization

Samples were sectioned with SiC cut-off wheels along the transversal (X-Z) and longitudinal (Y-Z) directions using the Discotom-2 and Accutom-10 (Struers, Copenhagen, Denmark). The cut sections were then hot-mounted in conductive carbon-filled bakelite resin (PolyFast, Struers) using the Hydropress A (Jean Wirtz, Düsseldorf, Germany). Before microstructural analysis, the samples were ground using SiC papers on a PlanoPol-2 (Struers) and polished with diamond suspensions on a Phoenix 4000 system (Buehler, Düsseldorf, Germany) according to the parameters listed in Table 3.4. Final polishing was completed with 0.04 µm colloidal silica to achieve a mirror-like surface finish.

SiC/Grain	P320	P600	P1200	P2500	6 µm	3 µm	1 µm	0.04 µm
Speed (rpm)	150	150	150	150	150	150	100	100
Time (min)	1–2	1–2	1–2	2–3	2–3	3–4	3–4	-

Table 3.4: Polishing parameters for microscopic observation.

Polished samples were cleaned with deionized water and ethanol, then dried using compressed air, followed by a hot air stream. This process minimized surface roughness and residual stress, enabling accurate microstructural, crystallographic, and chemical characterization via SEM, Energy Dispersive X-ray Spectroscopy (EDS), and Electron Backscatter Diffraction (EBSD). Analyses were conducted on cross-sections normal to the transverse direction (Y).

3.5.1 Optical Microscopy

Transversal (X-Z) cross-sections parallel to the build direction (Z) were used to observe the mesoscopic features and calculate the geometry of the single tracks following the dimensions listed in Fig. 3.9.

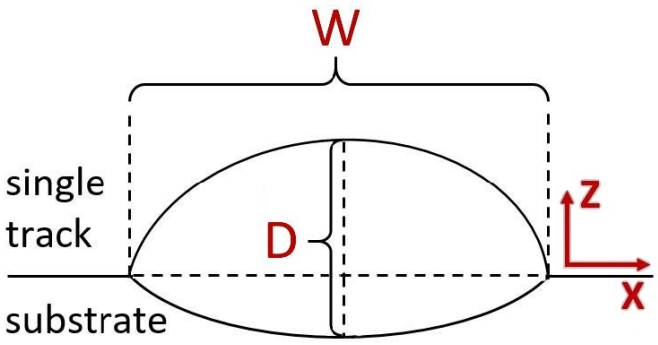

Figure 3.9: Single track transversal (X-Z) melt pool cross-section schematic with penetration depth (D) and width (W) marked.

The printed samples and their crystallographic morphology were observed with a ZEISS Axioplan optical microscope (Munich, Germany) and the S-neox 3D optical profilometer (Sensofar, Barcelona, Spain). Aqua regia etching solution (HCl: HNO_3 = 3:1) and the Contrast Limited Adaptive Histogram Equalization (CLAHE) was applied via the Fiji (ImageJ) image processing software to enhance features for observation. The CLAHE algorithm is an image processing technique designed to enhance local contrast by dividing the image into small regions or tiles, applying histogram equalization to each tile, and then combining them using bilinear interpolation [48]. The tile size used was 127 pixels, with 256 bins as seen in Code 2 of Appendix B.

3.5.2 Scanning Electron Microscopy

High-resolution SEM imaging was conducted using a Mira Tescan 3 (Brno, Czech Republic). Copper tape was applied near regions of interest on the sample cross-sections for electrical grounding. Imaging was performed in secondary electron (SE) and backscattered electron (BSE) mode from 15-20 kV acceleration voltage and approximately 1000 pA beam current. BSE imaging detects electrons reflected from the sample surface under electron-beam irradiation. The intensity of these backscattered electrons correlates with the atomic number of the constituent elements, resulting in brighter contrast for higher atomic number regions.

3.5.3 Energy Dispersive X-ray Spectroscopy

EDS analysis was carried out using an EDAX detector (Mahwah, NJ, USA) integrated into the Mira Tescan 3 SEM. Measurements were performed at an acceleration voltage of 20 kV and a beam current of approximately 2000 pA.

3.5.4 Electron Back Scatter Diffraction

The Ametek EBSD camera (Mahwah, NJ, USA) mounted on the Mira Tescan 3 SEM was used to characterize the samples' crystalline structure via phase distribution maps and the microstructural texture and grain orientation in the IPF, where the high-angle grain boundaries are indicated in black. All EBSD maps were created with a step limit of 0.3 µm and analyzed using OIMA software where the average grain diameter was calculated by isolating the melt pool grains as the Region of Interest (ROI).

3.5.5 Thermodynamic calculations

Thermodynamic calculations were performed using the TCFE7 database in Thermo-Calc and TC-Python to predict phase stability and potential precipitation behavior for Fe–Ti–O, Fe-Ti–N systems under the estimated thermal and compositional conditions of the melt pool. These results guided the interpretation of the observed microstructures, precipitate phases, and solidification behavior of both powder and substrate steel. The Scheil-Gulliver (S-G) calculations had C and N as fast-diffusing elements. The classic S-G model employs the following assumptions:

- Fast diffusion in liquid phase,
- Fast diffusion in solid phase for specified "fast diffuser" elements,
- No diffusion in solid phase for other elements,
- Thermodynamic equilibrium at S/L interface.

Chapter 4

Results and Discussion

This chapter begins with the results of the preliminary tests. The observations from these trials informed the structure and investigation of the parametric study on single tracks. The trends and phenomena observed are discussed in greater detail in the subsequent section.

4.1 Preliminary Tests

4.1.1 Characterization of Preliminary Tracks

Figure 4.1 shows the Light optical micrographs (LOM) of transversal cross-sections (X–Z plane) of two tracks deposited at NV 2000 mm/min: one without titanium injection (a) and one with Ti injected at Ti FR of 0.6 g/min (b). Representative metallographic cross-sections for each parameter set are included in Appendix A (Fig. 1).

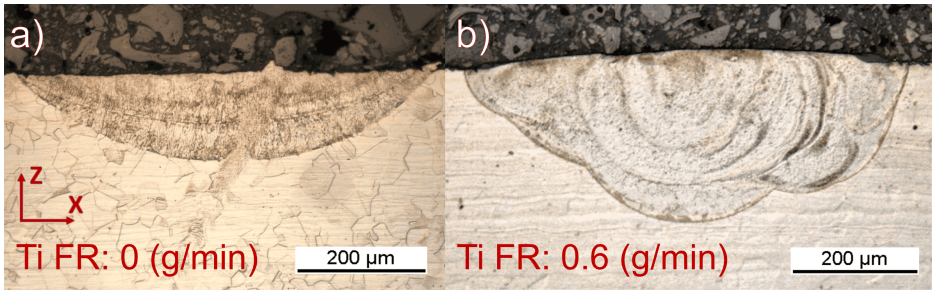

Figure 4.1: Transversal cross-sections (X–Z) of tracks at NV 2000 mm/min: a) without Ti injection, b) with Ti injection at 0.6 g/min.

The Ti-injected track exhibited a noticeably deeper melt pool, with distinct Ti-rich regions and melt pool vortices not observed in the Ti-free condition. A similar trend was observed in Fig. 4.2, which presents stitched longitudinal cross-sections (Y–Z plane) for tracks produced at 1500 mm/min, again comparing conditions without and with Ti injection. The track with no Ti injection in Fig. 4.2(a) was shallower with distorted grains starting from the melt pool boundaries, highlighted by the black dashed lines, trailing the moving heat source, as shown by the red arrows in the magnified section. The same process parameters with Ti injection in Fig. 4.2(b) produced a deeper melt pool with little to no distortions and significant grain refinement. The separate melt pool boundaries in the Ti FR 0.6, NV 1500 tracks are clearly visible, and present particle inclusions

and partially melted Ti regions circled in red.

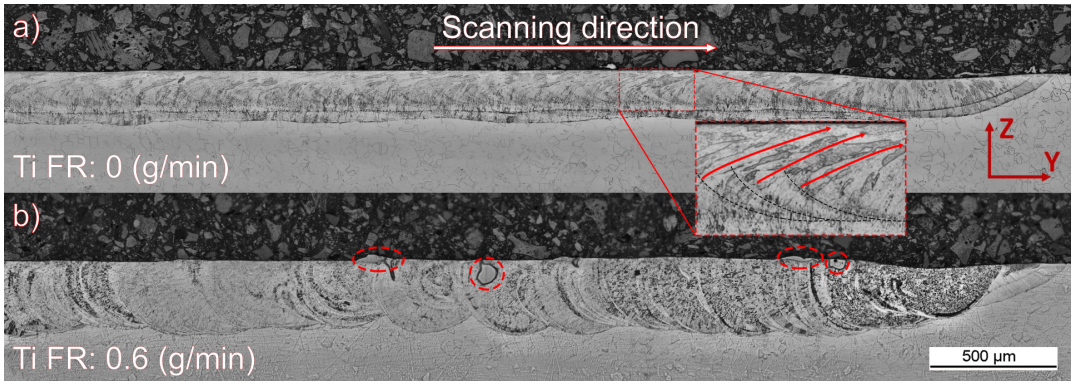

Figure 4.2: Longitudinal cross-sections (Y–Z) of tracks at NV = 1500 mm/min: a) without Ti injection, b) with Ti injection at 0.6 g/min. Ti inclusions are circled in red.

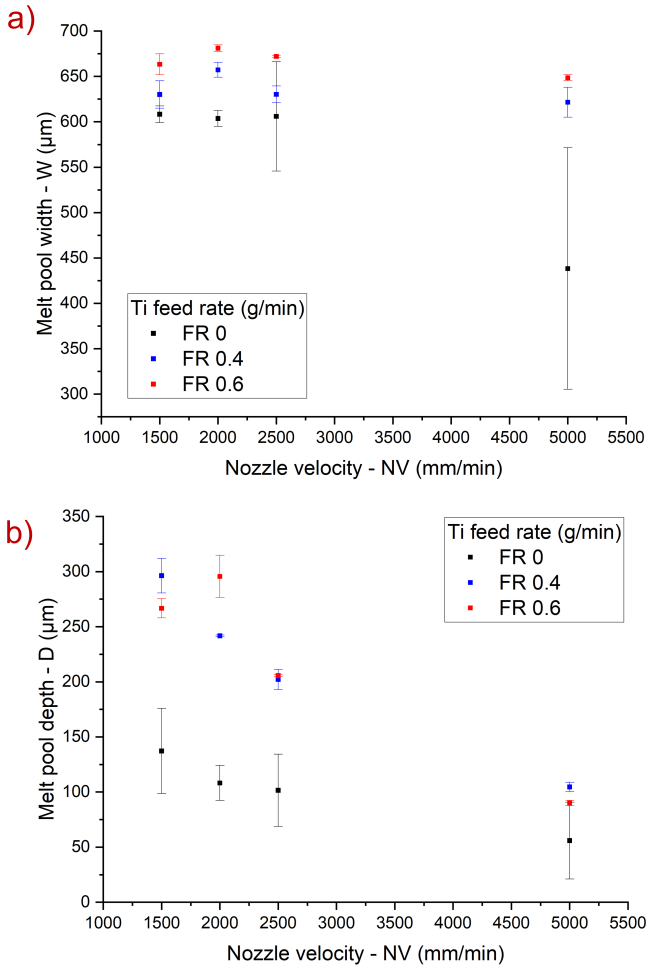

Figure 4.3: Measured melt pool dimensions for preliminary tracks at varying Ti feed rates: a) Width (W); b) Depth (D).

Quantitative optical measurements of melt pool width (W) and depth (D), based on the dimensional definitions introduced in Fig. 3.9, are summarized in Fig. 4.3. The large error bars are due to only two cross-sections being analyzed for the preliminary tracks samples. Across all tested conditions, Ti injection consistently resulted in an increased depth and a slight increase in width as hinted by the LOM observations.
Further details on the differences in the melt pool morphology were observed at higher magnification. Figure 4.4 presents transversal views of tracks deposited at NV 1500 mm/min, comparing Ti injection conditions.

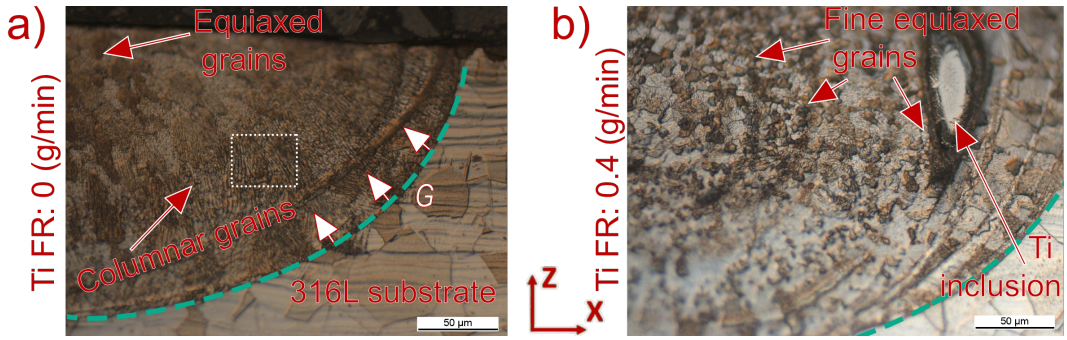

Figure 4.4: Transversal cross-sections (50x) of tracks at NV 1500 mm/min: a) without Ti injection, epitaxial grains with cellular structure; b) with Ti injection at 0.4 g/min, particle inclusion circled in red.

The Ti-free track in Fig. 4.4(a) shows a transformation of the substrate to a cellular substructure, highlighted by the white dotted area, within columnar grains. This is attributed to local Cr microsegregation, which appears as contrast variations following aqua regia etching. Heat transfer within the melt pool is spatially dependent: conduction dominates near the heat-affected zone at the lower boundary of the melt pool, which is outlined by the dashed teal lines in Fig. 4.4. In the central molten region, convection is prevalent, and a combination of conductive, convective, and radiative modes occurs at the lateral edges of the track, which are directly exposed to the environment. Microstructural features at the melt pool–substrate interface reveal steep and well oriented thermal gradients, illustrated by the white arrows. G is orthogonal to the melt pool boundary, promoting directional epitaxial growth inward from the edges. In contrast, near the center, where thermal gradients are lower and less directional, equiaxed grains seem to have formed. These could also be sectioned distorted epitaxial grains due to the moving heat source previously shown in Fig. 4.2(a). The G-driven solidification results in a hierarchical microstructure, characteristic of AMed A-SS [14]. As shown in Fig. 4.4(b), the addition of Ti at low nozzle velocities refines the microstructure, particularly around the dilution zone of partially melted Ti inclusions.

SEM imaging in BSE mode revealed a pronounced grain size reduction within the melt pool of the samples with added Ti particles compared to the cold-rolled 316L substrate,

as shown in Fig. 4.5(a). As mentioned, the BSE mode provides contrast based on the atomic number (z-number) of the sample. Materials with higher atomic numbers appear brighter because their heavier nuclei cause more elastic scattering of the incident electrons, while light compounds appear darker.

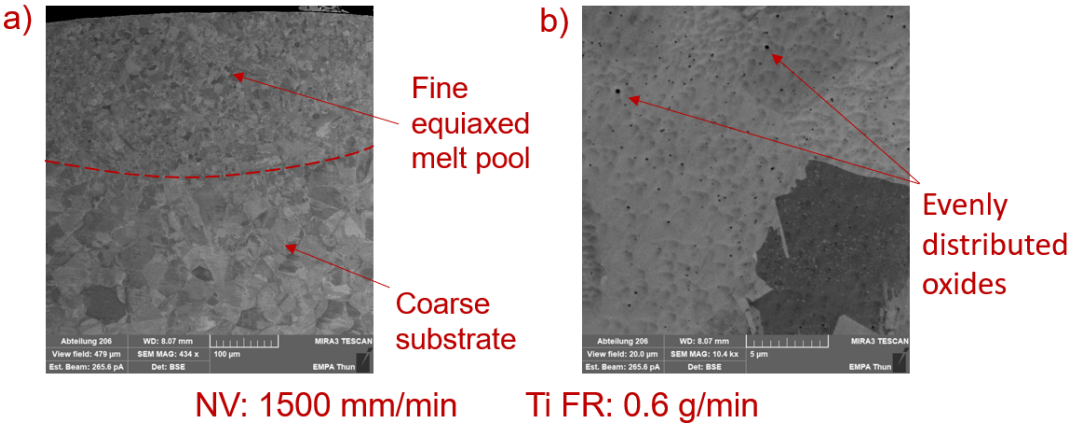

Figure 4.5: SEM-BSE images of the NV 1500 mm/min, Ti FR 0.6 g/min track. (a) Grain size contrast between the refined melt pool (outlined by the red dashed line) and the substrate; (b) Uniform dispersion of oxide and light-element particles within the melt pool grains.

All Ti injected melt pools exhibited a high density of dark sub-micron particles as shown in Fig. 4.5(b) for a representative track (NV = 1500 mm/min, Ti FR = 0.6 g/min).

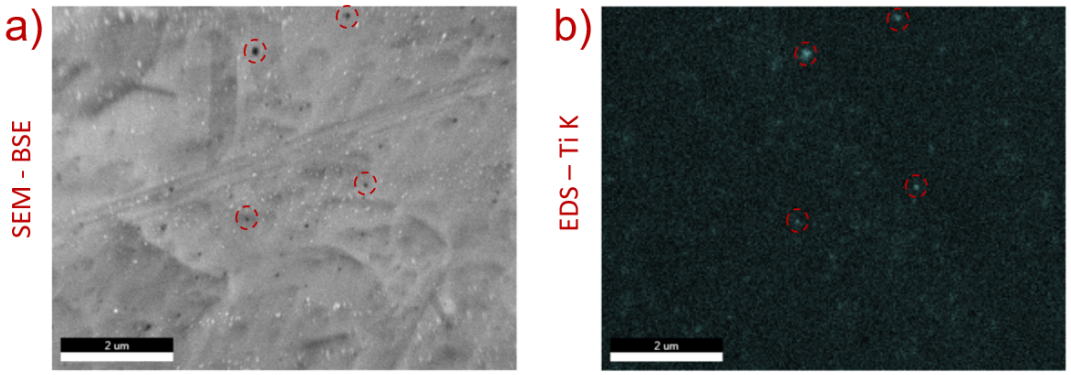

Figure 4.6: (a) SEM-BSE image highlighting Ti-rich oxides and light particles (red circles) in the melt pool of Fig. 4.5; (b) Corresponding EDS Ti Kα signal map for the ROI.

EDS measurements suggest that these are oxides enriched in Ti and other light-element inclusions, as shown in Fig. 4.6(b). When the ROI was expanded to characterize the entire melt pools, the Ti Kα signal closely matched the track geometry visible in the metallographic cross-section as illustrated in Fig. 4.7. Minor variations in local Ti content were detected for all tracks measured. In the Ti FR 0.6, NV 1500 track, the titanium concentration peaked at approximately 10 wt.% with an average of 5 wt.% Ti. This dis-

tribution indicates effective dilution of the injected Ti throughout the melt pool. These results, combined with the optical observations, lead to the confirmation of the hypothesis that the large G across the melt pool produced a fast Marangoni convection able to readily dilute the Ti particle.

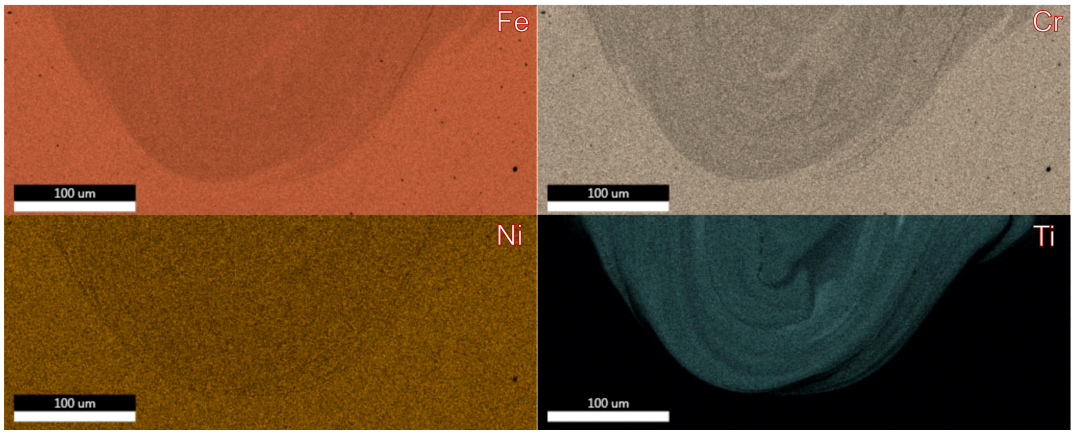

Figure 4.7: EDS Kα signal mapping of Fe, Cr, Ni, and Ti for the NV 1500 mm/min, Ti FR 0.6 g/min track.

4.1.2 Characterization of Preliminary Bulk Samples

Metallographic analysis of the preliminary bulk "sandwich" samples, composed of alternating 316L and Ti-enriched layers, revealed microstructural features consistent with those observed in the single-track experiments. These multilayer configurations may serve as an initial step toward the development of functionally graded materials, where properties are spatially tailored during the deposition process.

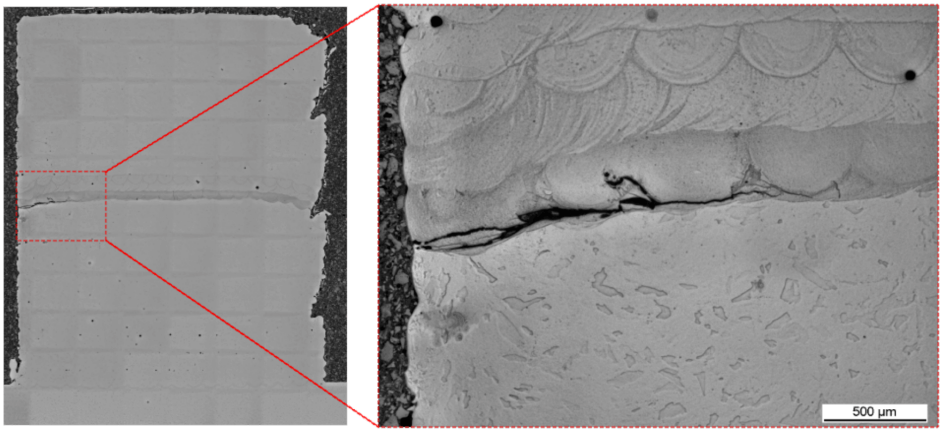

Figure 4.8: Optical micrograph showing cracking in the Ti layer of the sandwich sample deposited at NV = 2500 mm/min. The crack initiates at the outer edge and extends inward.

Significant grain refinement was observed in the Ti-rich layers, whereas the Ti-free

316L regions exhibited coarser grains as seen in the interface shown in Fig. 4.8. However, cracking was detected in the Ti layers deposited at NV = 2500 mm/min. As shown in Fig. 4.8, the crack initiated at the sample edge and propagated inward over approximately 2 mm, indicating it might be a cold crack. This failure is likely due to localized excess Ti, which may have led to compositional inhomogeneity and embrittlement. Additionally, thermal stresses resulting from the mismatch in coefficients of thermal expansion (CTE) between Ti-rich area and the pure 316L layers could have contributed to interfacial cracking, as described by Kou [23].

EBSD analysis on the preliminary sandwich samples confirmed significant grain refinement in the 316L layers near the Ti enriched layers. As shown in Fig. 4.9, both IPF and phase distribution maps indicate that the solidification mode is sensitive to processing conditions.

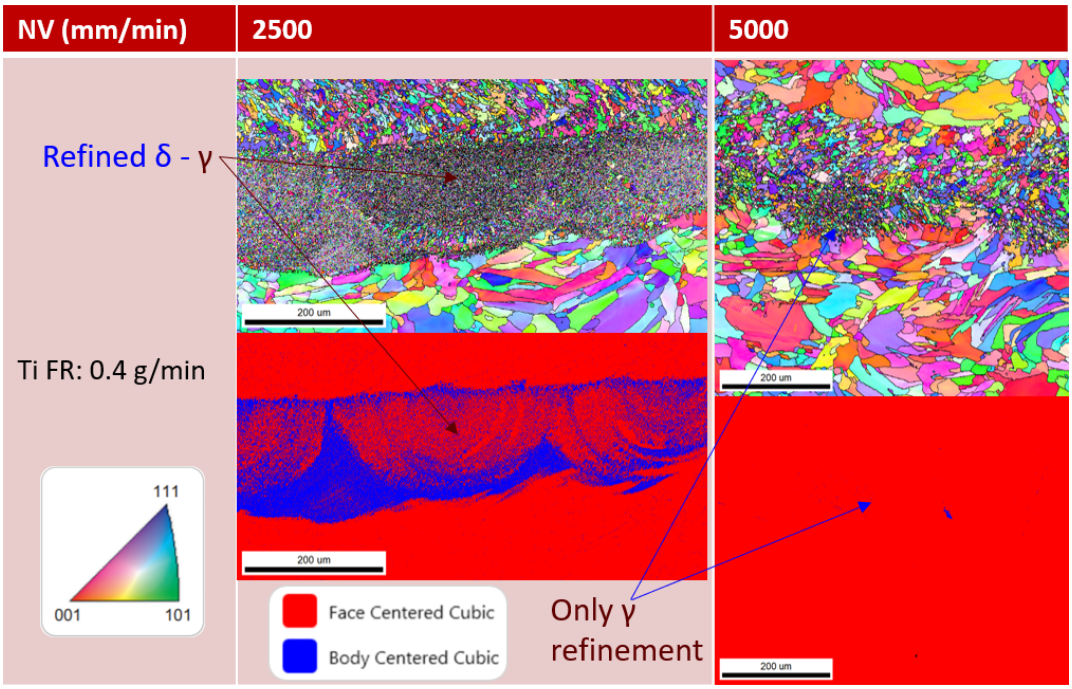

Figure 4.9: EBSD Inverse Pole Figure (IPF) colored maps and phase distribution maps showing the microstructure of the Ti FR 0.4 g/min layers of the sandwich samples at NV 2500 and 5000 mm/min .

The IPF maps show a transition from the coarse elongated grains in the pure 316L layers to fine equiaxed ones in the Ti-injected layers. The 316L layers present columnar grains with a length up to about 300 µm and a width of about 20–50 µm. The size of these grains, which in some cases are larger than the layer height of 200 µm, suggests that their growth could span across multiple melt pools, indicating that an epitaxial solidification arises during the building process. No preferential orientation was observed in the samples, probably due to the scanning pattern limiting the effect of G. As suggested in the previous section, the presence of texture in AM samples is strongly related to the

melt pool dimensions and, therefore, to the cooling conditions. Stronger textures are generally found in AM samples built with low energy densities (i.e., low power and high scan speed). The poor texture due to high energy density values is generally associated with the stronger turbulence of melt pools caused by the Marangoni flow [17]. The microstructure of the layers created by the Ti injection at NV 2500 mm/min resulted in the formation of a BCC phase in the FCC 316L, while the Ti-rich layers deposited at NV 5000 mm/min showed refined γ grains, larger than the mixed structure but with little to no BCC detected.

4.1.3 Key insights and takeaways

The characterization of these preliminary tests provided several insights into the microstructural effects of Ti injection:

- **LOM:** Etched tracks showed modified melt pool dimensions, Ti-rich swirls, particle inclusions, and a shift in grain morphology, from columnar epitaxial grains at the melt pool boundary to finer, equiaxed grains. Cracking was observed in the sandwich samples, likely due to excess Ti creating a local CTE mismatch between subsequent layers.
- **BSE Imaging:** Confirmed grain refinement within Ti-injected melt pools, with a high density of finely dispersed sub-micron oxides and light-element compounds.
- **EDS:** Identified these sub-micron compounds as Ti-rich. Ti appeared to be uniformly diluted across most melt pools, with localized enrichment.
- **EBSD IPF and Phase maps:** Revealed clear transitions from elongated grains to fine equiaxed ones in the sandwich samples between 316L layers and Ti-enriched regions, accompanied by significant grain size reduction. At Ti FR 0.4 g/min increasing NV promoted refinement of γ grains, while lower NV favored stabilization of a BCC phase within the FCC 316L matrix. Thus, the nozzle velocity and thereby the Ti deposition rate seem to influence the stable phases at room temperature, which suggests a shift in solidification mode driven by the high cooling rates and local compositional variations introduced by Ti injection. These aspects have been further discussed in Section 4.3.3.

Overall, Ti injection modified melt pool geometry and grain morphology, promoted phase stabilization shifts, and introduced particle inclusions as well as partially melted Ti regions. These observations motivated a systematic parametric study. Single-pass, non-rescanned (R0) tracks were used to examine melt pool size, grain refinement, and potential solidification mode transitions, while rescanned (R1) tracks were employed to reduce particle inclusions and inhomogeneities, thereby mitigating cracking.

4.2 Single Track Experiments

To investigate these phenomena over a wider operating range, three metallographic cross-sections for each parameter combination of the single-pass Ti injection tracks were produced and are shown in Fig. 2 of Appendix A. Representative transverse sections of the non-rescanned tracks (R0), shown in Fig. 4.10, revealed several trends.

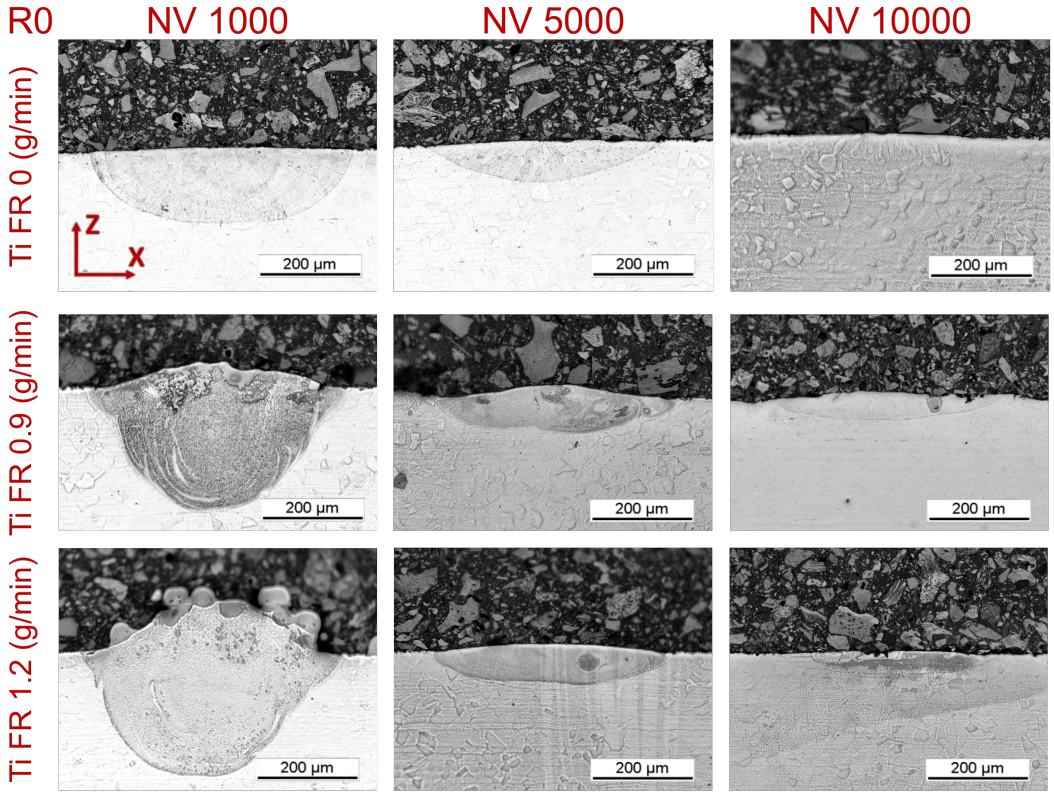

Figure 4.10: Representative X-Z cross-section of single pass non-rescanned (R0) tracks at deposition speeds (NV) 1000, 5000, 10000 mm/min with varying Ti FR.

The Ti FR 0 tracks exhibited grain morphologies consistent with the preliminary observations. Melt pool boundaries expanded radially and nearly symmetrically from the laser incidence point, showing little to no perturbation even at high NV. By contrast, Ti-injected tracks displayed pronounced asymmetry, with Ti-rich swirls and vortices. At low NV, both Ti FR 0.6 and 1.2 g/min tracks developed irregularly shaped melt pools containing Ti particle inclusions and Ti-rich regions. As expected, increasing the Ti FR to 1.2 g/min further intensified the occurrence of inclusions and partially melted Ti particles. The combination of high Ti FR and low NV additionally produced cracks, which were absent in the preliminary tracks. These cracks are most likely caused by excessive local Ti enrichment, where inclusions and Ti-rich regions (e.g., Ti FR 1.2 at NV 2000 in Fig. 2) are local inhomogeneities with a different coefficient of thermal expansion and

can act as stress concentrators during solidification.

The melt pool dimensions of the R0 tracks were averaged over the three replicates available for each parameter combination. Error bars in Fig. 4.11 represent the standard error (SE) of the mean. The measured melt pool sizes are consistent with those identified in the preliminary tracks, proving the process repeatability over the parameter range investigated.

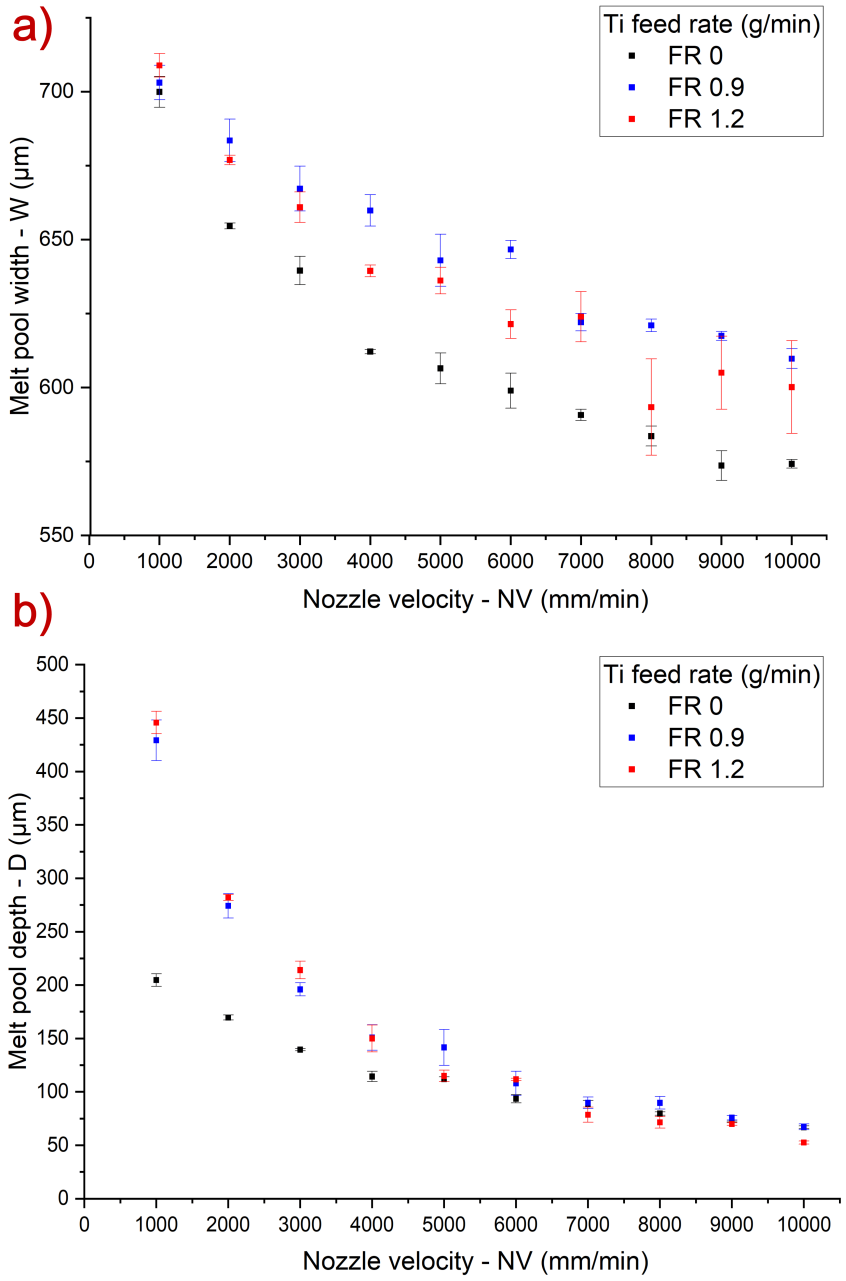

Figure 4.11: a) Mean melt pool depth (D); b) mean melt pool width (W) for non-rescanned (R0) track samples at varying Ti feed rates.

With increasing NV, a substantial reduction in average melt pool depth variation is noted: while lower speeds (1000–5000 mm/min) showed significant increases in D (ranging from 110% to 27%), this effect diminishes at higher NV due to reduced resident time of the nozzle over the melt pool. The Ti injected tracks displayed in Fig. 4.10 and Fig. 2 suggest that at high NV some areas appeared to be completely Ti free, resulting in a convergence with the Ti FR 0 depths as shown in Fig. 4.11 (b). The high SE values observed for the Ti FR 1.2 g/min samples in Fig. 4.11 are due to substantial variability, likely caused by cracking and subsequent material loss during mechanical preparation of the metallographic samples.

To evaluate the effects of Ti injection on grain size and phase distribution, EBSD analysis was performed on the non-rescanned (R0) samples, as shown in Fig. 4.12. The figure shows a representative sample of EBSD IPF and phase distribution maps of R0 tracks deposited at increasing NV from left to right and decreasing Ti injection feed rate top to bottom.

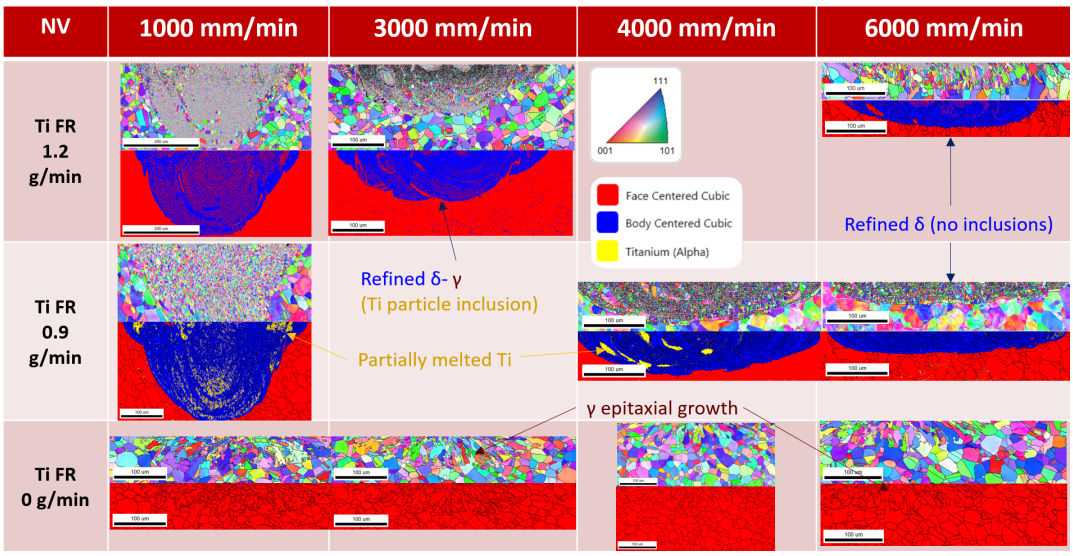

Figure 4.12: IPF and phase distribution maps showing γ (FCC), δ (BCC), and alpha titanium for non-rescanned (R0) tracks at increasing NV and varying Ti FR.

In the IPF maps of the Ti-free tracks (Ti FR 0), columnar grains were consistently observed, originating from the bottom of the melt pool and extending radially inward. This morphology is well documented and results from the combination of a high G, oriented normal to the melt pool boundary, and comparatively low R at the melt pool boundary, promoting preferential growth of grains aligned with the thermal gradient [4, 17, 27]. The solidified structure in these Ti-free samples is fully austenitic, with no detectable BCC, consistent with the AF solidification mode of the 316L substrate depicted in Fig. 2.4. Despite the EDS line scans and mapping performed showing local variations in the Ti wt.% occasionally exceeding the eutectic composition of 14 wt.%, no Fe_2(Ti,Nb)

Laves phase was observed in any of the examined tracks. The high cooling rate and rapid solidification of DED processing probably limited the time interval the melt spent in the Laves forming temperature region.

Figure 4.13 shows the average melt pool grain diameter as a function of the increasing NV for the R0 tracks with varying Ti FR. Due to time constraints, only one sample for each parameter combination underwent EBSD mapping and subsequent grain size analysis. As previously discussed in Section 2.3.1, the cooling rate $\dot{T}$ influences the size of the final structure. Increasing NV from 1000 to 5000 mm/min shortened beam residence time, raising $\dot{T} = G \times R$ and inducing modest grain refinement of approximately 10% in the Ti-free samples.
As a rule of thumb:

Faster scan speed $\uparrow V_{NV} \rightarrow \uparrow G, \uparrow \dot{T} \rightarrow$ reduced melt pool $\downarrow$ D $\downarrow$ W, finer grains.

Slower scan speed $\downarrow V_{NV} \rightarrow \downarrow G, \downarrow \dot{T} \rightarrow$ enlarged melt pool: $\uparrow$ D $\uparrow$ W, larger grains.

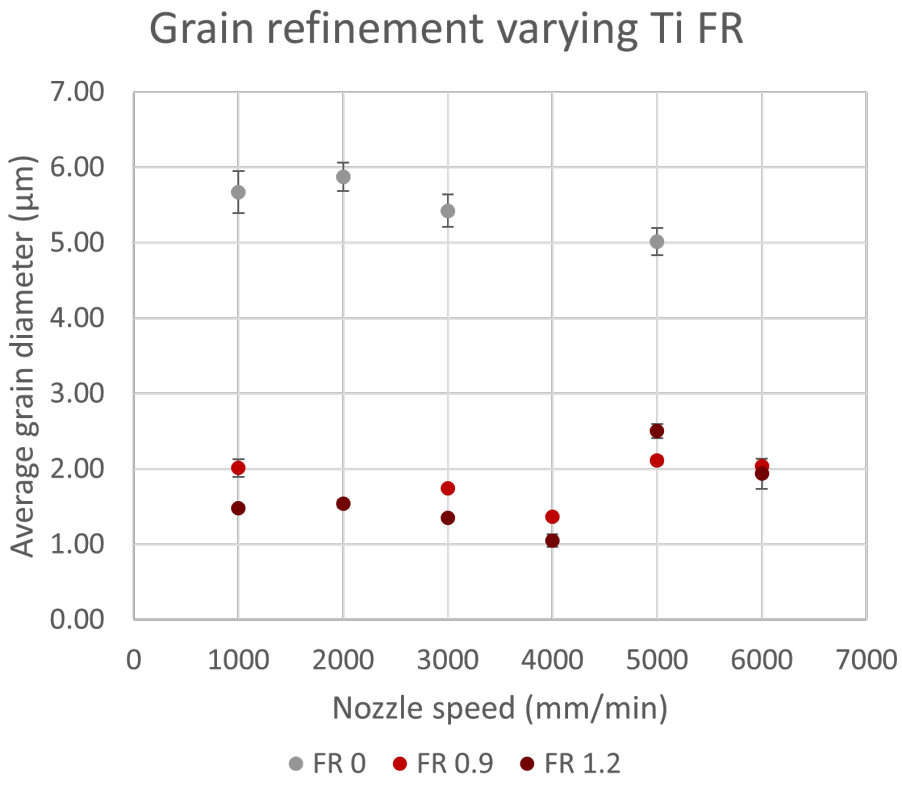

Figure 4.13: Average grain size diameter within the melt pool for single-pass (R0) tracks at varying Ti injection feed rates.

In line with previous optical microscopy observations, Ti injection resulted in the formation of Ti-rich regions and partially melted Ti inclusions. These areas of the tracks consistently exhibited significant microstructural refinement and the presence of BCC, independent of the speed or feed rate used during deposition.
For the Ti FR 0.9 tracks (light red dots in Fig. 4.13) with NV 1000, 3000, and 5000 mm/min the reduction in grain size was 64.5%, 67.8%, and 57.8%, compared to the Ti free tracks as shown in Table 4.1. While the Ti FR 1.2 g/min tracks presented a slightly finer microstructure with up to 75.1% reduction in the average grain diameter, higher NV further reduced the amount of Ti entering the melt pool, thereby reducing the grain refinement effects of the particle injection as can be observed for the NV 5000 and 6000 mm/min tracks.

Ti FR (g/min)	NV (mm/min)	Avg. grain diameter (mm)	Grain size change (%)
0	1000	5.67 ± 0.28	–
0	3000	5.42 ± 0.21	–
0	5000	5.02 ± 0.18	–
0.9	1000	2.01 ± 0.12	-64.5
0.9	3000	1.75 ± 0.04	-67.8
0.9	5000	2.11 ± 0.05	-57.8
1.2	1000	1.48 ± 0.04	-73.9
1.2	3000	1.35 ± 0.03	-75.1
1.2	5000	2.50 ± 0.10	-50.1

Table 4.1: Average grain diameter and grain size change under different Ti feed rates (FR) and nozzle velocities (NV).

The LOM and SEM analyses all confirmed the presence of swirls and melt pool perturbations in the Ti injected R0 tracks.

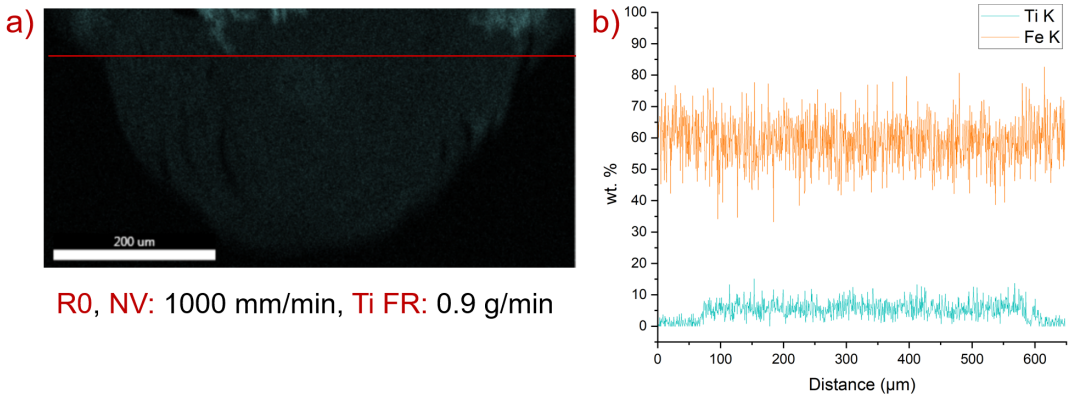

Figure 4.14: a) Ti Kα signal from EDS mapping of the track R0, NV 1000 mm/min, Ti FR 0.9 g/min; b) Fe and Ti wt.% following line scan (red) across the track melt pool.

EDS mapping revealed these vortices, possibly created by rapid Marangoni convection

flows (Section 4.3.1), to be rich in titanium with slight concentration variations across the melt pool.

Taking the NV 1000 mm/min, Ti FR 0.9 g/min track as an example, the EDS line scan shown as the red line in Fig. 4.14 displayed fluctuations in the Ti content with a peak of approximately 15 wt.% and an average of around 5 wt.%. This compositional inhomogeneity of the track compared to the surrounding substrate could be the reason behind the presence of the BCC ferrite phase at room temperature in the A-SS.

Analysis of the local Cr_{eq}/Ni_{eq} ratio (Eq. 2.1) in several tracks suggests that Ti injection altered the substrate's solidification mode (Table 2.1) shifting from the AF to the FA range, and ultimately to the F mode in regions with the highest Ti concentration. This progression is supported by the phase distribution data in Fig. 4.15(a) showing the FCC γ, BCC δ, and Alpha Ti in red, blue, and yellow, respectively. Figure 4.15 (b) further illustrates the Cr_{eq}/Ni_{eq} profile across the melt pool alongside the corresponding predicted solidification modes.

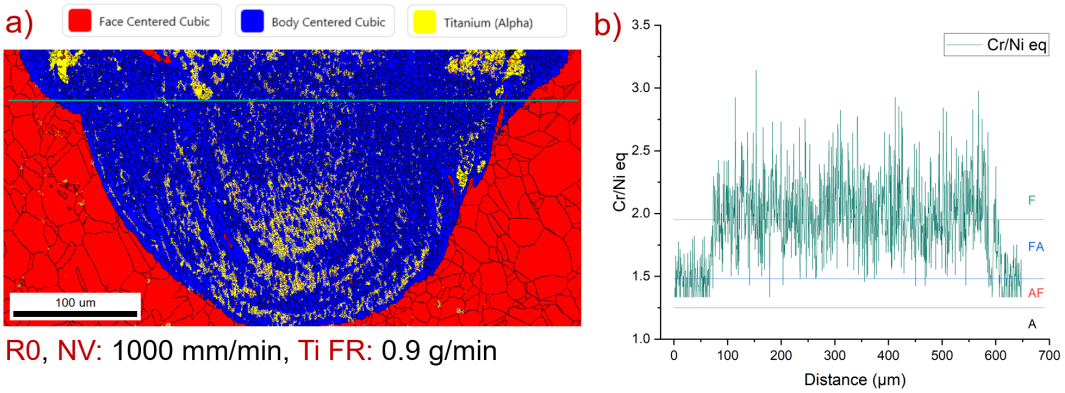

Figure 4.15: a) EBSD phase distribution map of track R0, NV 1000 mm/min, Ti FR 0.9 g/min with EDS line scan in teal; b) Predicted solidification mode with Cr_{eq}/Ni_{eq} calculated from line scan data. Horizontal lines indicate the different solidification thresholds as described in Table 2.1: A austenitic, AF austenitic–ferritic, FA ferritic–austenitic, F ferritic .

Ti content is lowest at the edges of the melt pool, where the Cr_{eq}/Ni_{eq} values indicate an AF solidification path. Analogously to the Ti-free tracks, the rapid solidification conditions could have favored primary γ formation, resulting in a fully austenitic microstructure in those regions, as no δ was detected within the EBSD 0.3 µm step limit applied.

4.2.1 rescanned Tracks

While higher Ti feed rate promoted greater grain refinement, it also led to an increased formation of unmolten Ti inclusions. These inclusions at low NV and high Ti FR were investigated through EBSD and EDS mapping. As shown in the IQ map in Fig. 4.16, these

inclusions display notable characteristics under EBSD analysis.

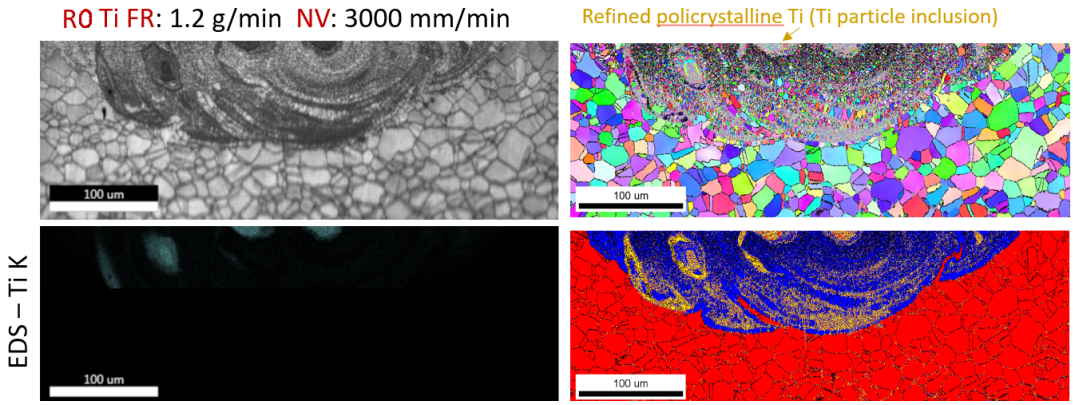

Figure 4.16: IQ, EBSD, EDS Ti-Kα and phase distribution maps of a track with NV 3000 mm/min and Ti FR 1.2 g/min, showing Ti inclusions and dilution with the surrounding microstructure.

Whereas the feedstock Ti powder typically consists of single or few-crystal particles, the polycrystalline nature of the inclusions observed suggests that they underwent partial melting followed by rapid in-situ solidification. Additionally, the surrounding matrix exhibits a dilution zone with modified composition, which appears to embrittle the 316L and is associated with crack initiation and propagation. To mitigate these effects, a rescanning strategy was incorporated into the parametric study. The rescanned track samples (R1) consisted of applying a second melting pass at the same NV as the initial Ti injection one. The goal was to promote dissolution of partially melted particles, enhance Ti homogenization within the melt pool, reduce cracking susceptibility, and simulate the thermal cycling effects of subsequent layers.

Figure 3 in Appendix A provides an overview of all the R1 samples for varying Ti feed rates, illustrating their influence on melt pool morphology and inclusion behavior. As shown in the representative cases in Fig. 4.17, in the Ti FR 0.9 tracks, rescanning at NV above 3000 mm/min did not fully homogenize the Ti inclusions formed during the injection pass, nor did it alleviate the cracking phenomena. Similarly, while Ti FR 1.2 g/min tracks exhibited a reduced inclusion count compared to their single-pass counterparts, significant cracking was still observed at low NV values (1000–5000 mm/min). This is likely due to the excessive local Ti concentration and the limited mixing capability of the melt pool when rescanning is performed at the same NV as the injection pass.

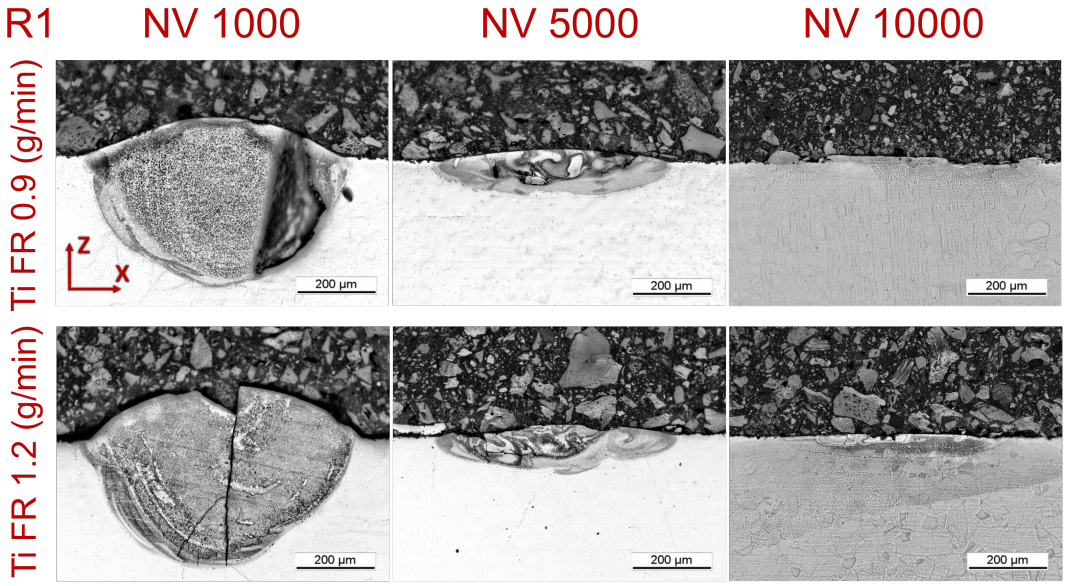

Figure 4.17: Representative cross-sections of rescanned (R1) tracks at deposition speeds (NV) 1000, 5000, 10000 mm/min with varying Ti FR.

Since lower FR values led to incomplete or non-continuous turn-plate revolutions per minute (RPM) 0.6 RPM, corresponding to 0.9 g/min, was used as the practical lower limit for consistent Ti feed rate. Consequently, the most effective strategy to reduce overall Ti input while preserving injection consistency was to increase the nozzle velocity. Higher NV values reduce melt pool volume and residence time, thereby limiting Ti dissolution. It is well known that Marangoni forces are active during AM, which will cause rapid fluid flow and mixing within the melt pool [17, 40, 42]. This mixing will continue as long as the heat source is present, but once the heat source passes, the melt may thermally equilibrate before complete solidification.

Among all tested conditions, tracks deposited at NV 6000 mm/min showed the most favorable combination of Ti dispersion, consistent injection, and crack-free morphology. This makes them the most promising candidates for further optimization, particularly through rescanning passes conducted at lower NV than the initial injection to improve homogenization by taking advantage of the Marangoni convection.

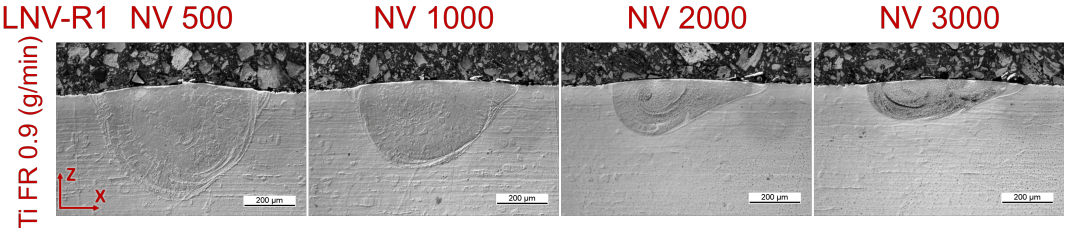

Figure 4.18: Representative metallographies of low NV rescanned tracks (LNV-R1) with Ti FR 0.9 g/min.

Tracks were rescanned at NV of 500, 1000, 2000, and 3000 mm/min. None of the tested conditions exhibited cracking, partially melted Ti or retained Ti inclusions. These observations promote the hypothesis that rescanning at lower NV than the injection pass is effective in mitigating these microstructural defects. The reduced NV increased the melt pool residence time and slightly enlarged the remelted zone beyond the original injected track, as visible in Fig. 4.18.

The IPF and phase maps from the EBSD analysis of the LNV-R1 tracks have been summarized in Fig. 4.19. Observing the phase distribution maps, the microstructure of the regions remelted at lower NV appears to remain primarily ferritic (BCC). Notably, the tracks rescanned at NV 500 mm/min displayed larger γ grains near the melt pool boundary, likely due to partial remelting of the unalloyed 316L substrate. Higher nozzle speed resulted in an almost fully ferritic structure, or at least higher ferrite fraction in comparison with the lower nozzle speeds, as the shorter diffusion time possibly limited the solid state $\delta \rightarrow \gamma$ transformation upon cooling.

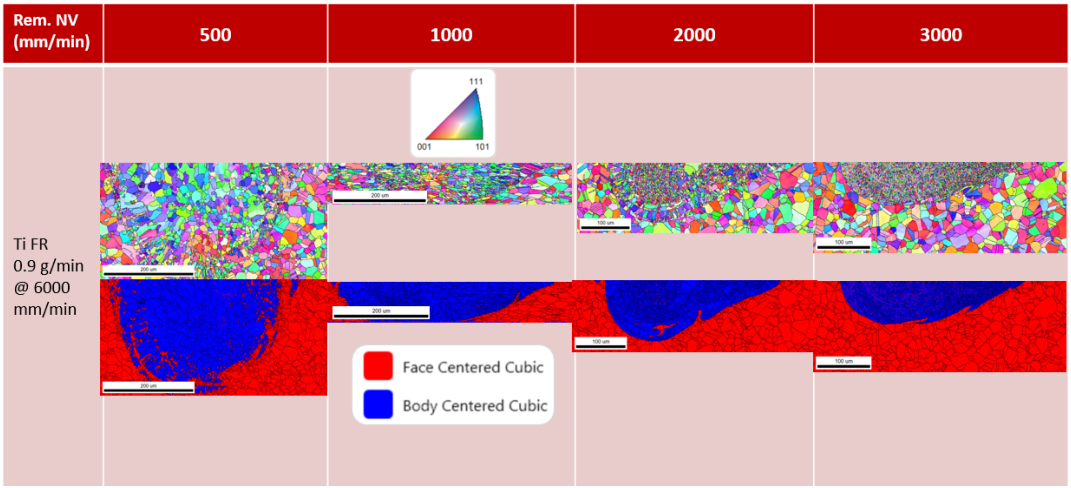

Figure 4.19: IPF and phase distribution maps showing γ (FCC), δ (BCC), and alpha titanium for low NV rescanned (LNV-R1) tracks at low rescanning nozzle velocities.

Naturally, decreasing the rescanning NV lowers $\dot{T}$, resulting in slightly coarser grains compared to the single-pass (R0) track. This phenomenon is illustrated in Fig. 4.20, which compares average grain sizes across both processing approaches. The effect of the grain coarsening seems to stop around NV 2000-3000 mm/min.

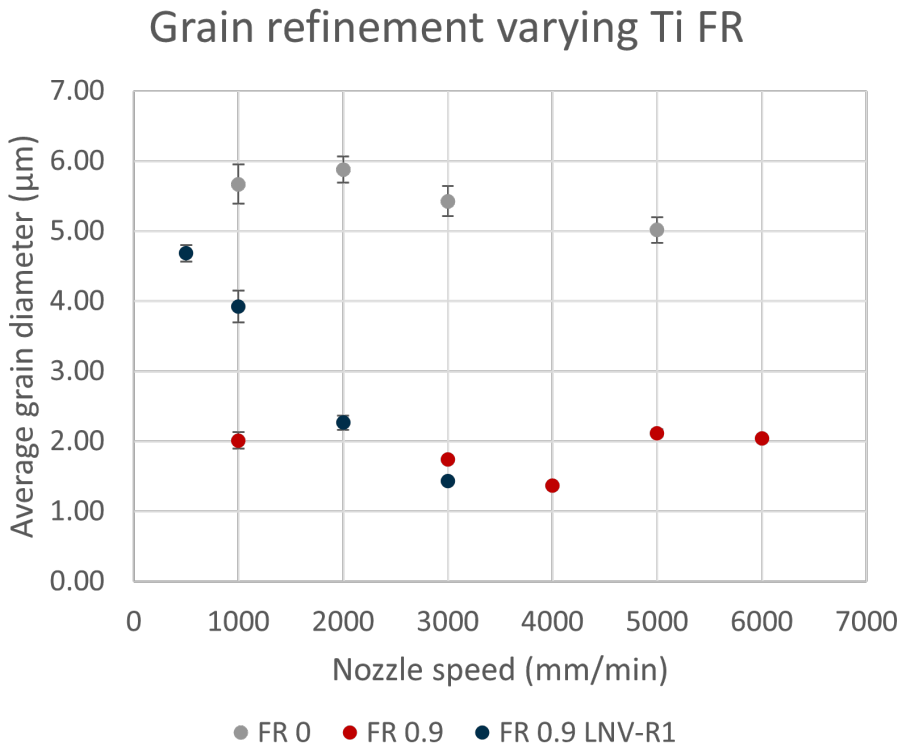

Figure 4.20: Average melt pool grain size diameter comparison between single-pass (R0) tracks and low NV rescanned tracks (LNV-R1) for the same Ti FR 0.9 g/min.

4.3 Discussion

4.3.1 Melt Pool Size Alterations

In both the preliminary tests and the parametric study, the injection of Ti showed significant effects on the melt pool dimensions. The melt pool size is primarily correlated to the NV through the Linear Energy Input (LEI) experienced by the substrate, which can be expressed as a function of the laser power (P), substrate absorptivity (α), and nozzle speed (V_{NV}):

$$\text{LEI} = \frac{P\alpha}{V_{NV}} (\text{J/mm}) \tag{4.1}$$

Laser power P was kept constant at 300 W for all samples. Figure 4.3 and Fig. 4.11 show that at slower speeds, both melt pool W and D increased for almost all tracks due to the increased LEI. Also in the LNV-R1 tracks (Fig. 4.18), reducing NV increased the volume of molten material. Interestingly, the melt pool dimensions show a strong sensitivity to any Ti injection. Aggarwal et al. [40] demonstrated that, during DED, Ti particles interacting in-flight with the laser beam can produce a shadowing effect on the substrate as shown in Fig. 4.21.

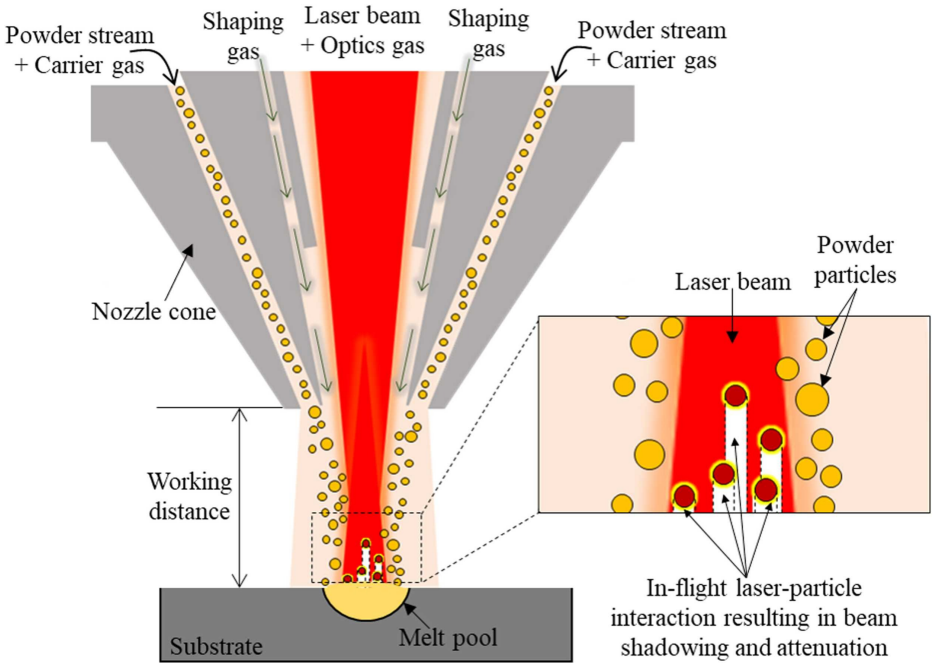

Figure 4.21: Schematic of the coaxial laser-based directed energy deposition process. The magnified view shows the laser-particle interaction, which results in beam attenuation and shadowing [40].

The injection of Ti particles modifies the interaction between the laser and melt pool, potentially altering the effective energy distribution and deviating from the Gaussian thermal profile typically observed in Ti-free tracks. Under such conditions, a reduction in thermal input would normally be expected due to partial laser shadowing by the injected particles. Although this effect may have been limited by the short working distance of 3.5 mm, tracks fabricated at identical NV values with and without Ti injection should, in principle, experience a constant laser energy input (LEI) and produce melt pools of comparable size.

Contrary to this expectation, experimental results showed that at low NV and high Ti FR, the melt pool depth nearly doubled, despite the anticipated attenuation. This indicates that additional mechanisms must be contributing to the increased thermal input and/or altered melt pool dynamics.

One plausible explanation lies in compositional effects on α. As expressed in Eq. (4.1), an increase in α would raise the effective energy input to the substrate.

Based on these values, it is unlikely that the observed increase in melt pool volume can be explained by bulk absorptivity differences alone. A more plausible explanation involves the rapid in-flight oxidation of Ti, which produces Ti-rich oxides, consistent with both experimental observations [40] (Fig. 4.6) and Thermo-Calc predictions for the Fe–Ti–O–N system (Fig. 4.23). Dense oxide films are known to enhance absorption through multiple secondary reflections, in contrast to the predominantly single-direction reflec-

tion from the Ti-free substrate [49]. Although the expected levels of oxygen uptake are unlikely to cause the formation of such a dense film.

Furthermore, the introduction of surface-active species, particularly oxygen and sulfur, is known to modify the temperature coefficient of surface tension, $\left(\frac{d\sigma}{dT}\right)$ even in extremely low quantities (ppm). This coefficient governs Marangoni convection in the melt pool [42, 43, 44] as variations in $\frac{d\sigma}{dT}$ can alter flow regimes, potentially leading to deeper melt pools and modified solidification dynamics, as schematically illustrated in Fig. 4.22.

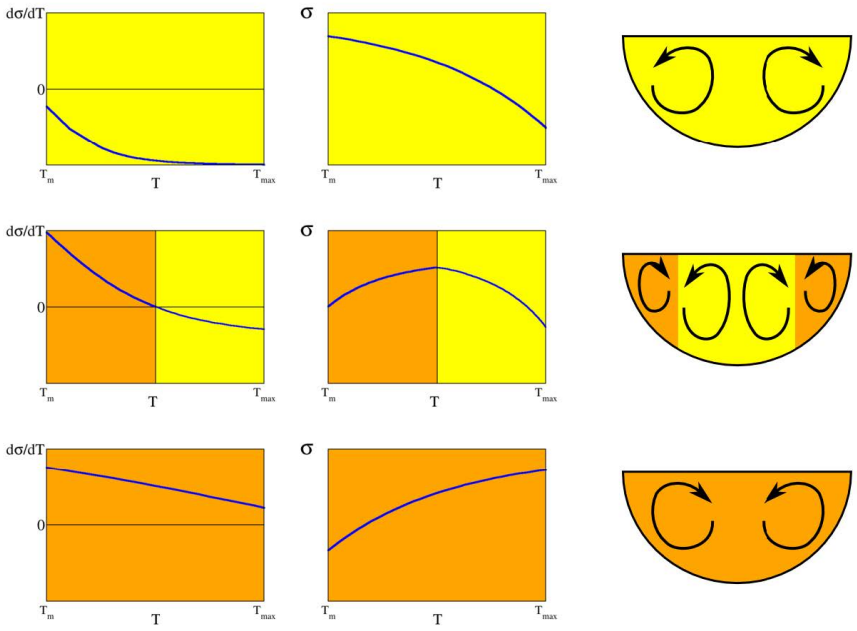

Figure 4.22: Schematic of the relationship between surface tension gradient $\left(\frac{d\sigma}{dT}\right)$ and Marangoni-driven flow directions for different surface-active element concentrations [43].

The three characteristic flow regimes influenced by surface-active element concentrations include:

- **Negative $\frac{d\sigma}{dT}$ (low S/O content):** Surface tension decreases with temperature, resulting in an outward flow from the hot pool center toward the cooler periphery.
- **Transitional regime (medium S/O content):** $\frac{d\sigma}{dT}$ is positive at the cooler pool edge and negative at the hot center. Counter-rotating flows form and meet at a radial location where $\frac{d\sigma}{dT} = 0$.
- **Positive $\frac{d\sigma}{dT}$ (high S/O content):** Surface tension increases with temperature, driving inward flows from the pool edge toward the center.

Variations in $\frac{d\sigma}{dT}$ can thus strongly affect weld pool shape, size, and the resulting microstructure. Prior studies have shown that increases in the S or O ppm content can substantially enlarge the melt pool volume at a given energy input by both reversing the flow direction and increasing the flow velocity [42, 43, 44]. Increasing the alloying elements in a metal tends to lower its melting point, as seen in Fig. 2.7. Thus, alloying 316L with Ti lowered the melting point of the substrate, as later confirmed by the Thermo-Calc simulations in Fig. 4.26. The synergy between this effect and the Marangoni flow changes is the probable cause for the increase in melt pool size observed at low NV and high Ti FR. While the ability to exploit this effect for process optimization, by tailoring internal melt flow through surface-active element control, has been recognized, a full parametric analysis was considered beyond the scope and timeline of this project.

4.3.2 Effects of Ti injection on grain morphology

The injection of Ti consistently produced a change in the grain morphology of both the 316L substrate and powder. In both tracks and bulk samples, Ti injection resulted in a transition from coarse columnar grains, growing epitaxially from the melt pool boundary to randomly oriented fine equiaxed ones. The addition of any Ti in the tracks resulted in the melt pool showing a BCC phase at room temperature. The sandwich samples conversely showed the possibility of obtaining a refined γ based on the process parameters used, which in turn controlled the Ti concentration in the layers. The primary hypothesis of this project was to modify in-situ the A-SS microstructure through the formation of known Ti-rich refiners, which combined with the solutal effects of Ti would suppress epitaxial growth and promote grain refinement via heterogeneous nucleation following the mechanism illustrated in Fig. 2.9. This tailoring approach initially seemed plausible given that all the tracks and sandwich samples where titanium was injected presented Ti-rich precipitates similar to the ones shown in Fig. 4.6.

Thermo-Calc was used to predict the likely compositions of the Ti-rich precipitates observed in the melt pool. Partial isoplethal sections for the (Fe,O)–Ti and (Fe,N)–Ti systems (Fig. 4.23) were calculated using estimated oxygen and nitrogen concentrations of 0.22 wt.% and 0.03 wt.%, respectively, based on the 316L substrate composition and literature data [22].

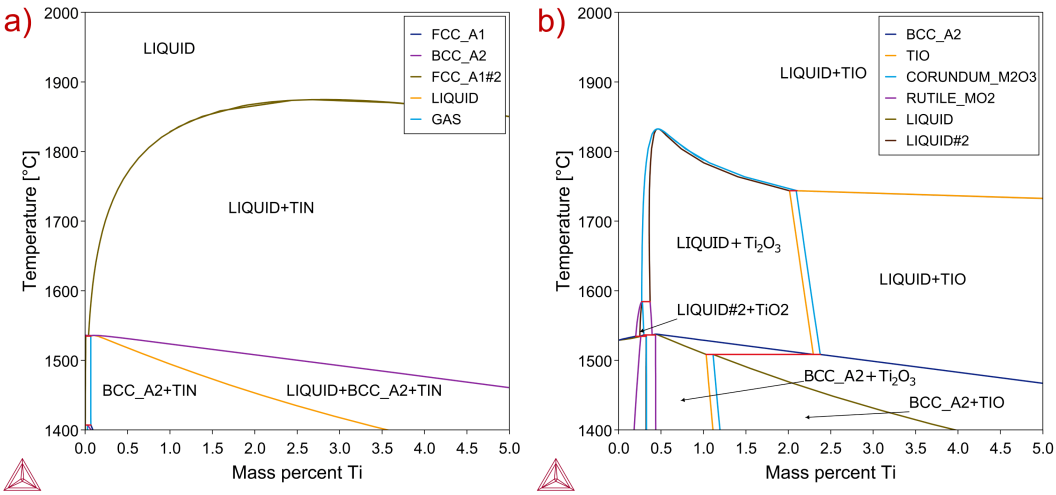

Figure 4.23: Ternary equilibrium phase diagrams for (a) Fe–N–Ti (0.03 wt.% N) and (b) Fe–O–Ti (0.22 wt.% O) systems generated using Thermo-Calc, based on 316L composition and literature estimates [22].
Note: FCC_A1#2 = TiN, CORUNDUM_M2O3 = Ti_2O_3, RUTILE_MO2 = TiO_2.

The simulation in Fig. 4.23(a) predicts the precipitation of an ordered FCC structure (FCC_A1#2), corresponding to titanium nitride (TiN), at any Ti content. The isoplethal section in Fig. 4.23(b) indicates the formation of different titanium oxides depending on the Ti wt.%. Considering the average Ti content of 5 wt.% in the melt pool (Fig. 4.7), the precipitates observed in Fig. 4.6 are expected to be TiO, Ti_2O_3, and TiN. A definitive confirmation would require other advanced characterization techniques such as high-resolution transmission electron microscopy (HRTEM) combined with selected area electron diffraction (SAED), which could more precisely identify these precipitates and reveal potential orientation relationships with the surrounding grains. However, such analyses were beyond the scope of this project.

EBSD analysis consistently showing the presence of a ferritic BCC phase in all Ti-injected tracks, regardless of NV or Ti FR, suggested that the grain refinement measured for the R0 tracks in Fig. 4.13 may not only result from the hypothesized TiN and TiC precipitation but also from a shift in the solidification mode of the substrate as hinted by the Cr_{eq}/Ni_{eq} analysis shown in Fig. 4.15.

4.3.3 Substrate Solidification Behaviour

To validate whether Ti addition can shift the solidification mode of the substrate and identify the BCC as either α or δ-ferrite, a series of thermodynamic simulations was conducted, beginning with the Ti-free areas as a baseline. Figure 4.24(a) shows the equilibrium phase evolution of the 316L substrate during cooling, based on its nominal composition from Table 3.1. The composition of the system was defined as consisting

mainly of Cr (17.5 wt.%), Ni (11.5 wt.%), smaller additions of Mo (2.25 wt.%), Mn (2.0 wt.%), and trace amounts of C (0.025 wt.%) and N (0.11 wt.%) with Fe as balance.

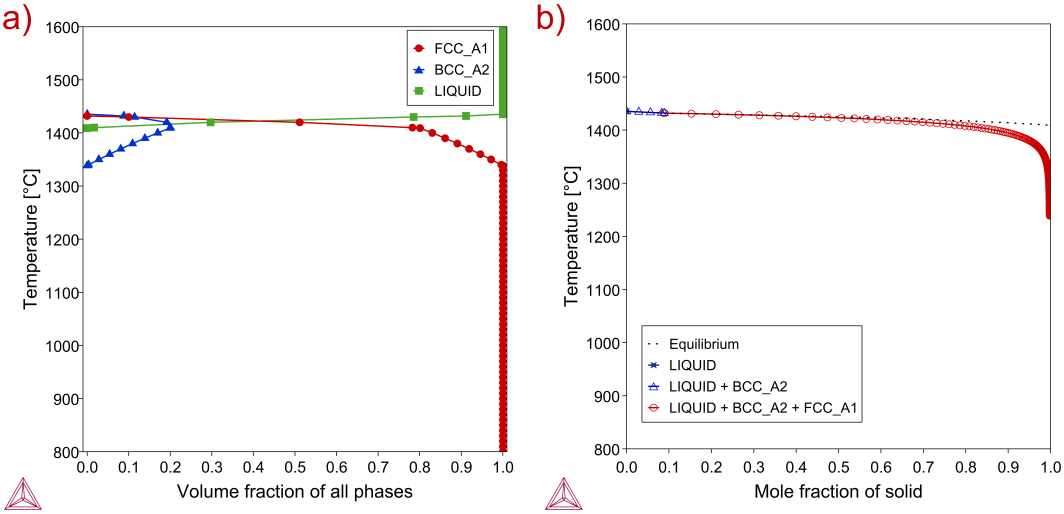

Figure 4.24: Thermodynamic predictions for Ti-free nominal substrate composition (Table 3.1): (a) equilibrium phase fractions upon cooling; (b) Scheil–Gulliver non-equilibrium solidification model. C and N treated as fast-diffusing elements.

Solidification begins at approximately 1440°C with the near-simultaneous formation of δ (BCC_A2) and the complete transformation of the liquid around 1410°C. As cooling proceeds, the δ fraction decreases steadily, disappearing near 1340°C, leaving a fully austenitic structure at lower temperatures.

While these equilibrium predictions indicate phase stability under slow cooling, the rapid solidification conditions of AM can lead to δ retention and microsegregation. To address this, Fig. 4.24(b) presents the non-equilibrium solidification path calculated using the S–G model, under the assumptions detailed in Section 3.5.5.

The S–G model predicts primary δ formation ($L \rightarrow \delta_{prim.}$) at 1435°C, followed shortly by γ nucleation at ∼1430°C, consistent with the FA solidification mode described in Table 2.1. Solidification terminates with both δ and γ phases present; however, the S–G model does not account for subsequent solid-state transformations. The absence of any BCC phase in the microstructure of the Ti FR 0 tracks in Fig. 4.12 is therefore likely due to a combination of the peritectic reaction ($L + \delta \rightarrow \gamma$) and the direct $\delta \rightarrow \gamma$ solid-state transformation during cooling [21].

For the Ti-free substrate, Thermo-Calc predicts FA solidification, in contrast to the AF mode inferred from the Cr_{eq}/Ni_{eq} diagram in Fig. 4.15(a). This discrepancy can be explained by small deviations in local chemistry. As indicated by the red dashed line in Fig. 2.4, the nominal composition of the 316L substrate lies near the AF/FA transition boundary, making the Cr_{eq}/Ni_{eq} classification highly sensitive to compositional fluctuations. Additionally, the strong chemical affinity of Ti for Ni can lead to the formation

of ordered NiTi phases, which deplete Ni from the steel matrix. NiTi is typically present as nano-precipitates detectable only by TEM or high-resolution X-ray diffraction, techniques not available in this study. While direct evidence of this phase was not obtained, its possible presence could shift the local Cr_{eq}/Ni_{eq} ratio toward values favoring ferrite stabilization.

To model the Ti-enriched regions analogous simulations, shown in Fig. 4.25(a-b), were conducted adding a Ti content of 5 wt.% to the system composition, as determined from the EDS line scan in Fig. 4.14(b).

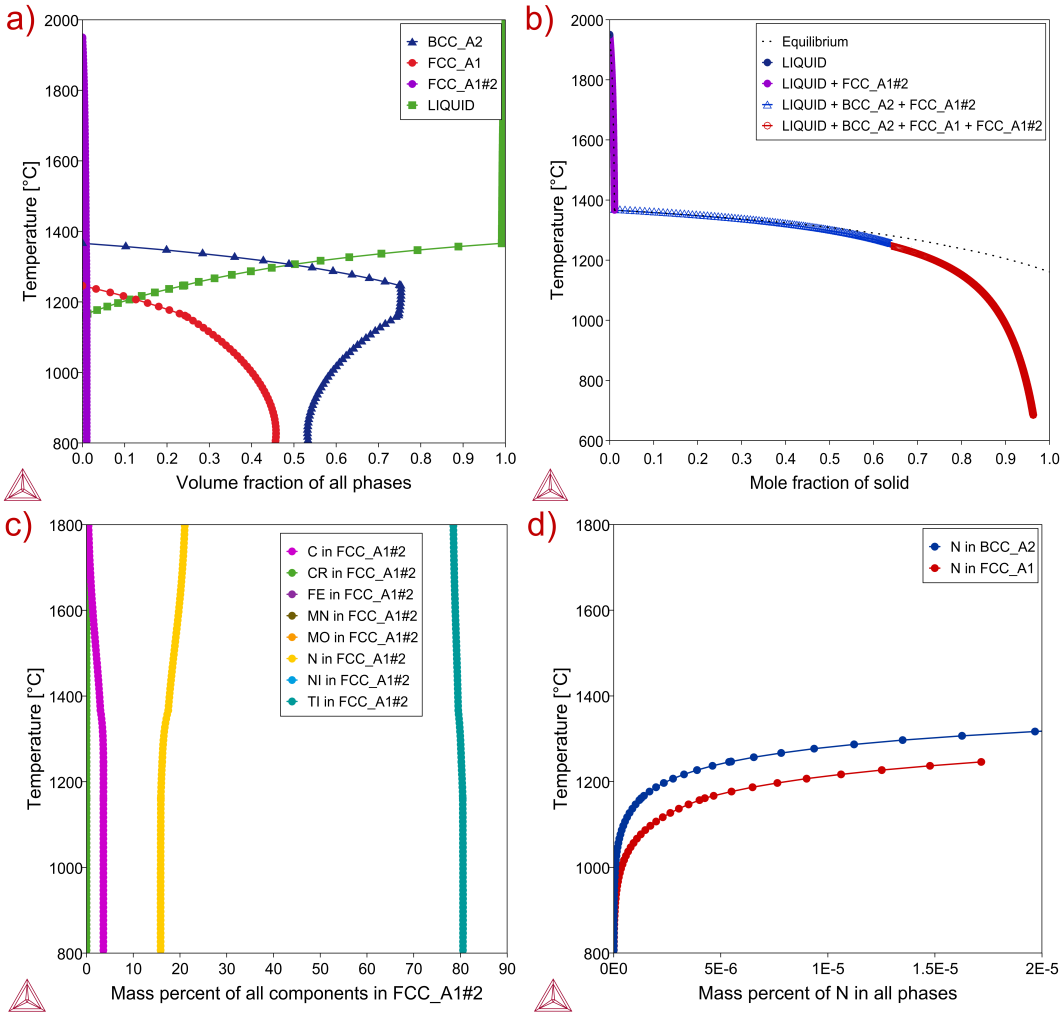

Figure 4.25: Thermodynamic calculation for 316L substrate with 5 wt. % Ti a) equilibrium phase fraction upon cooling; b) Classic Scheil-Gulliver non equilibrium solidification. C and N are fast diffusing; c) FCC_A1#2 equilibrium composition evolution; d) Equilibrium nitrogen concentration in δ and γ. **Note:** FCC_A1#2 = TiN and TiC.

The equilibrium results for the Ti modified 316L in Fig. 4.25(a) indicate the following key differences with the previous simulation:

- Formation of $\delta_{prim.}$ at 1366°C,
- Coexistence of δ, γ, and liquid over a broad temperature range $\sim$1245–1160°C,
- High thermal stability of FCC_A1#2, consistent with the ternary phase diagram in Fig. 4.23(a).

Both equilibrium and S-G simulations predict the precipitation of the ordered FCC_1#2 phase prior to primary δ solidification from the high-temperature liquid, followed by austenite formation via the peritectic reaction between δ and liquid. The chemical composition of the FCC_1#2 phase is shown in Fig. 4.25(c). This ordered precipitate contains approximately 80 wt.% Ti, 16 wt.% N, and 4 wt.% C, indicating the formation of TiN and TiC, both of which are well-established grain refiners for stainless steel [20, 21, 37]. For simplicity, oxygen was not included in the calculation, as it is absent from the certified composition in Table 3.1, and the formation of TiO and Ti_2O_3 had already been predicted in the ternary diagram in Fig. 4.23(b).
Although the present calculation does not explicitly address the competitive precipitation of oxides, nitrides, and carbides, the high reactivity of Ti, combined with the relatively low O/Ti mass ratio, suggests that the formation of TiO and/or Ti_2O_3 would not suppress subsequent TiC or TiN precipitation. Nitrogen, a strong γ stabilizer with high affinity for Ti, is expected to be rapidly consumed by TiN formation during the early stages of solidification. This process could locally deplete the γ matrix of nitrogen, thereby increasing the Cr_{eq}/Ni_{eq} ratio and potentially shifting the solidification mode. However, given the low nitrogen content in the 316L substrate (≤ 0.11 wt.%) and the absence of post-print nitrogen measurements, the magnitude of this effect is considered minimal, as indicated in Fig. 4.25(d).

These results support the hypothesis that, under local equilibrium conditions at the S/L interface, Ti injection shifts the solidification regime from δ and γ forming almost simultaneously from the liquid, to a $\delta_{prim.}$ condition. The BCC observed in the EBSD phase distribution for the Ti injected tracks can thus be inferred to be retained δ-ferrite. As shown in Fig. 4.26, the Ti injection seems to have increased the amount of δ present upon solidification following the S-G simulations in Fig. 4.24 (b) and Fig. 4.25 (b). The effect of the addition of Ti in the tracks, according to the Thermo-Calc simulations performed, could be summarized as follows:

(i) Precipitation of TiN, TiC at $\sim$1940°C and TiO, Ti_2O_3 at $\sim$1940°C (Fig. 4.23(b)),

(ii) Promotion of $\delta_{prim.}$ formation and shift to FA solidification mode.

(iii) Change in the nucleation temperature of δ from $\sim$1435 to 1365°C,

(iv) Increase in the retained δ molar fraction upon solidification from $\sim$32% to 79%.

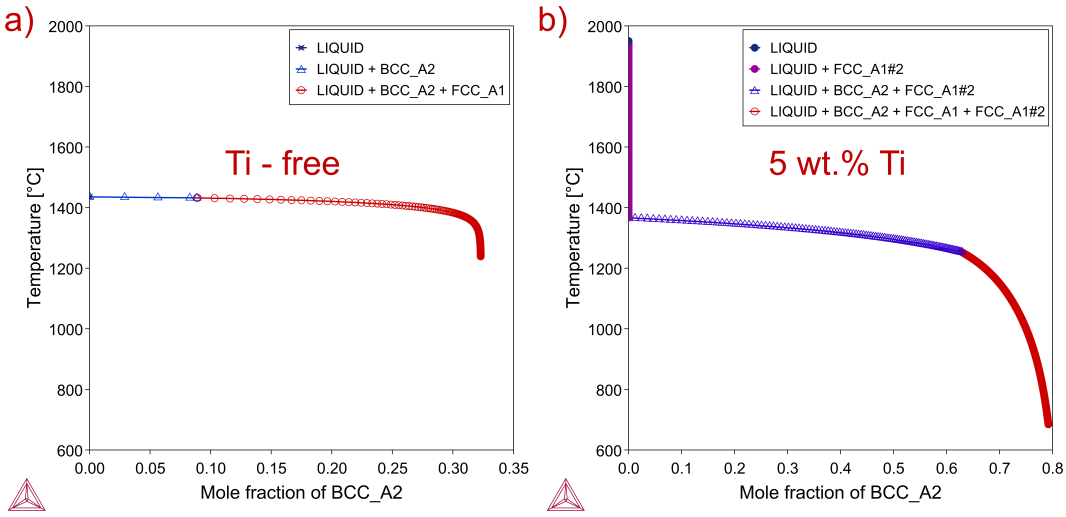

Figure 4.26: Mole fraction of δ upon S-G model solidification for a) Ti-free substrate, b) substrate with addition of 5 wt.% Ti.

Merging the observations made during characterization of the samples with the results discussed in this section, it's possible to expect the injection of titanium to have produced grain refinement via the combination of TiN and TiC precipitation and a shift in the solidification mode.

Attempts at in-situ refinement on the 316L substrate resulted in all the alloyed tracks exhibiting a significant volume fraction of undesired δ precipitation. However, when the matrix composition was slightly modified, as in the 316L powder used for the sandwich samples, a refined austenite structure was achieved. This indicates that when applying this process for the fabrication of a component, close control of the alloy chemistry and the Ti addition would be crucial to achieve the desired microstructural tailoring and avoid deleterious effects on the mechanical and corrosion properties.

Chapter 5

Conclusions

5.1 Summary of Key Findings

The present work investigated the influence of in-situ titanium injection during L-DED of 316L stainless steel on process stability, microstructural evolution, and phase development. The main conclusions are as follows:

1. **Process parameter optimization:** A systematic study of nozzle velocity (NV) and titanium feed rate (Ti FR) identified process windows capable of producing defect-free single tracks. Crack-free deposits were consistently obtained by depositing at NV of 6000 mm/min and Ti FR up to 0.9 g/min with a subsequent rescanning pass at NV between 500–3000 mm/min, where stable powder delivery and melt pool geometry were maintained. At lower NV combined with high Ti FR, excessive particle inclusions and altered melt pool flow led to cracking and high particle inclusions, whereas at high NV, low Ti injection was observed.

2. **Marangoni convection effects:** The addition of Ti lowers the melting point of the substrate and leads to the formation of Ti-rich oxides, likely increasing oxygen content in the melt pool. The increased presence of surface-active elements such as oxygen has been shown to alter the temperature dependence of surface tension $\left(\frac{d\sigma}{dT}\right)$, potentially reversing or transitioning Marangoni flow. Such a change in melt pool convection, combined with the decrease in melting temperature, could explain the observed increase in penetration depth at low NV and high Ti FR despite anticipated shadowing effects.

3. **Phase constituents and solidification mode:** Thermo-Calc simulations and experimental phase analysis revealed that Ti addition modifies the local Cr_{eq}/Ni_{eq} ratio, shifting the solidification mode towards the ferritic–austenitic (FA) and ferritic (F) regime. The substrate composition when injected with any amount of Ti resulted in a completely ferritic structure at room temperature. Ti-rich oxide and nitride phases, particularly TiO, TiC and TiN, are likely to precipitate early in the solidification process. The early TiN precipitation, while serving as a potential nucleant, also depletes nitrogen from the matrix, further influencing phase stability.

4. **Grain refinement and texture changes:** EBSD analyses demonstrated that Ti injection promoted a change in the microstructural texture and a partial reduc-

tion in the average prior-γ grain size compared to the Ti-free tracks. The refinement effect was most pronounced at intermediate NV and higher Ti FR, where the Ti-induced phase change, combined with a uniform dispersion of Ti-based particles, could have triggered heterogeneous nucleation. Correspondingly, the strong $\langle 100 \rangle$ build-direction texture of the Ti-free material was weakened, indicating reduced anisotropy.

Overall, these findings highlight that controlled Ti injection during L-DED of 316L can not only refine grain structure but also alter solidification pathways and modify melt pool dynamics, offering a promising strategy for tailored microstructural engineering in additively manufactured stainless steels.

5.2 Future works

Future work should include EDS scans of all samples to precisely quantify the Ti concentration and the fabrication of tensile samples to evaluate the mechanical performance of the 316L processed via Ti injection. Additional sandwich samples, fabricated using the same parametric approach applied to the single tracks, could identify the process conditions under which the transition from δ stabilization to a fully γ structure occurs, though this would be time-intensive. Furthermore, expanding the multiphysics simulation of the DED process [40, 42], combining CFD and particle–melt interactions could provide valuable insight into how titanium injection influences flow dynamics and reverses Marangoni convection patterns. Additionally, the transport of the Ti across the melt could be coupled to TC Python to be able to predict the solidification behaviour of the melt pool, circumventing the time constraints of EBSD analysis. Advanced characterization techniques, such as High-resolution TEM (HRTEM) and selected area electron diffraction (SAED), could also be employed to precisely identify the Ti-rich precipitates observed in Fig. 4.6 and to examine their orientation relationships with the surrounding grains.

Appendix A

Supplementary Images

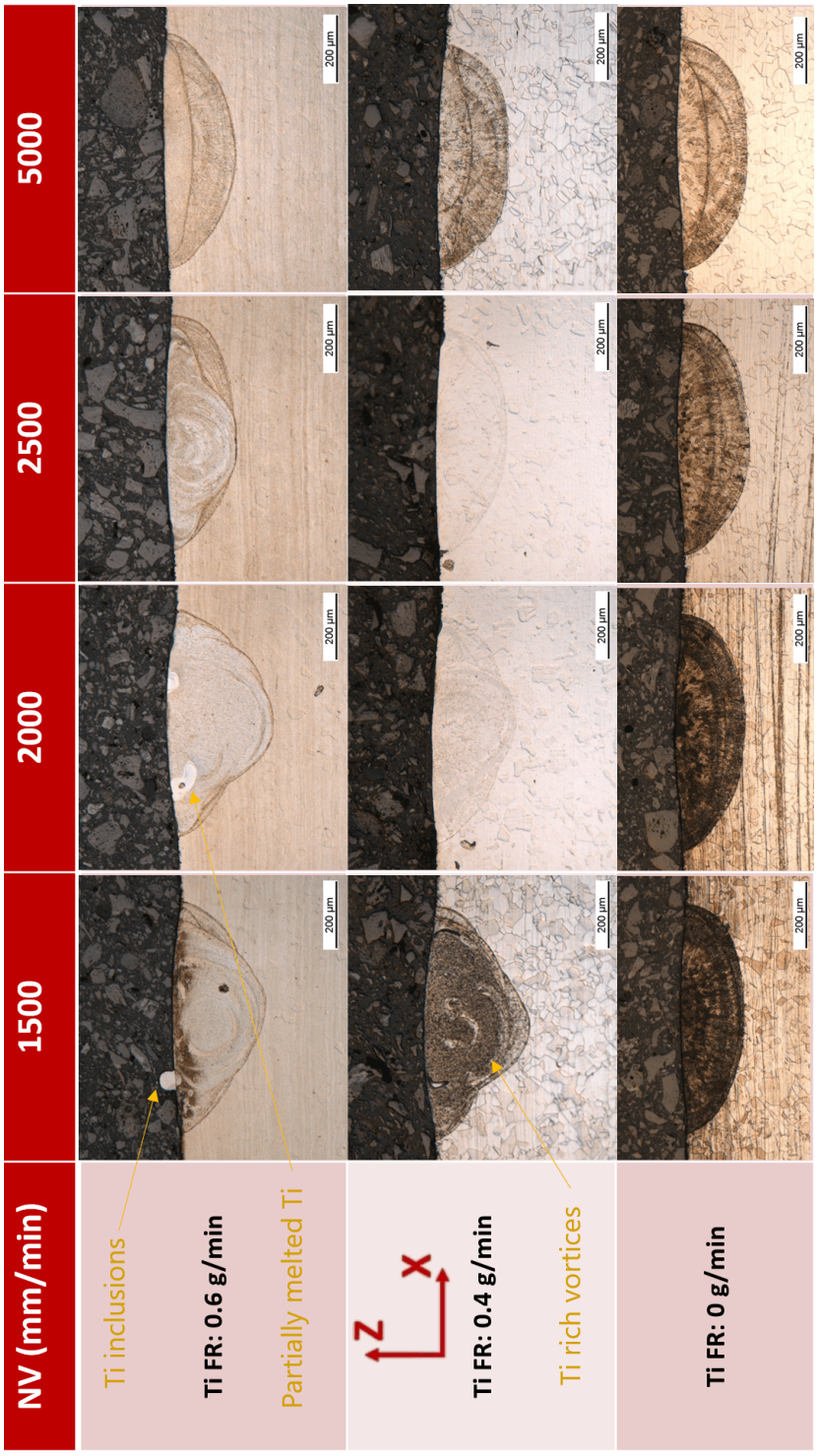

Figure 1: Optical transversal cross-sections of the preliminary single tracks with high, low, and no Ti injection feed rate (Ti FR) at varying nozzle velocities (NV).

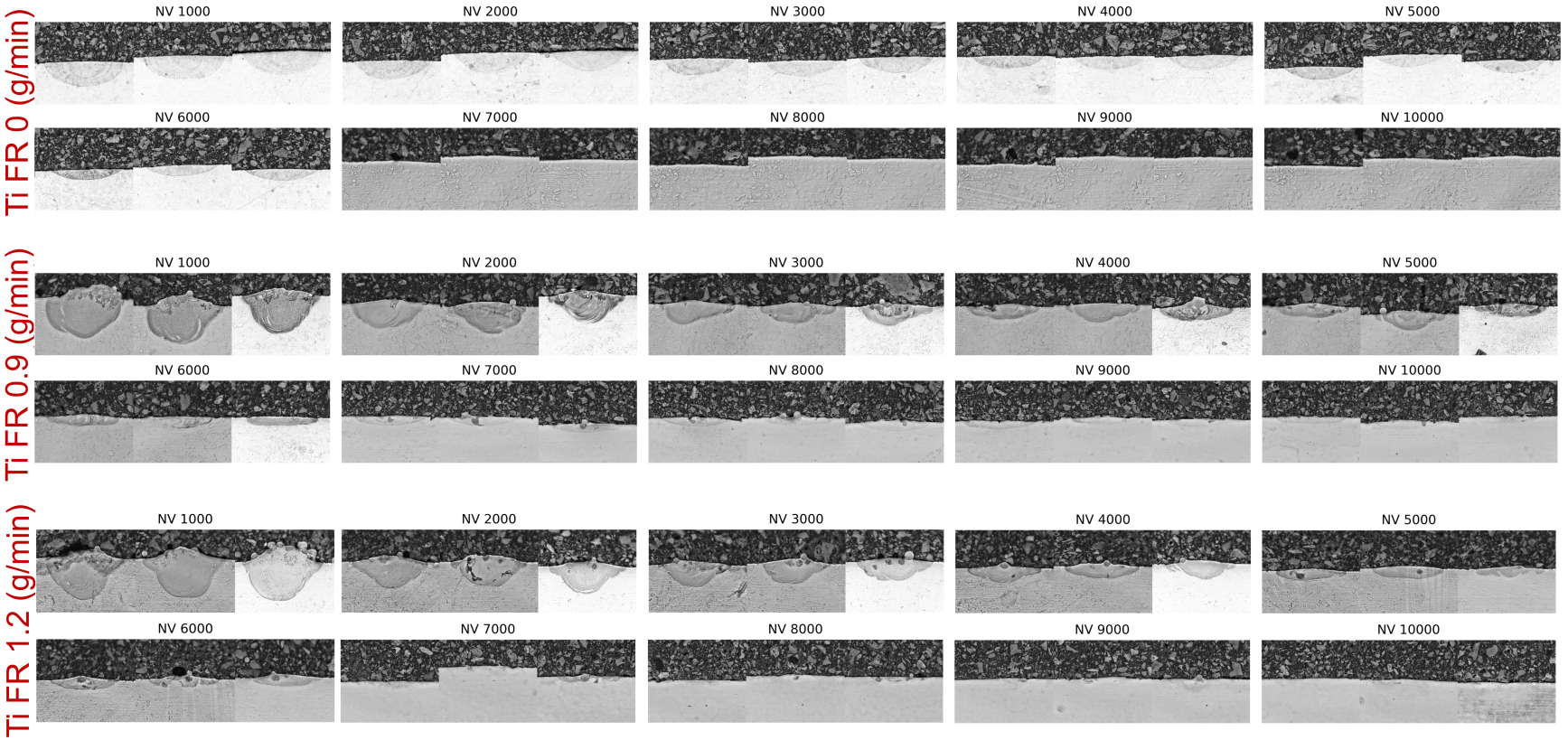

Figure 2: Optical transversal cross-sections of tracks with a single Ti injection pass (RO) of 0, 0.9, 1.2 g/min (Ti FR) and varying nozzle velocities (NV).

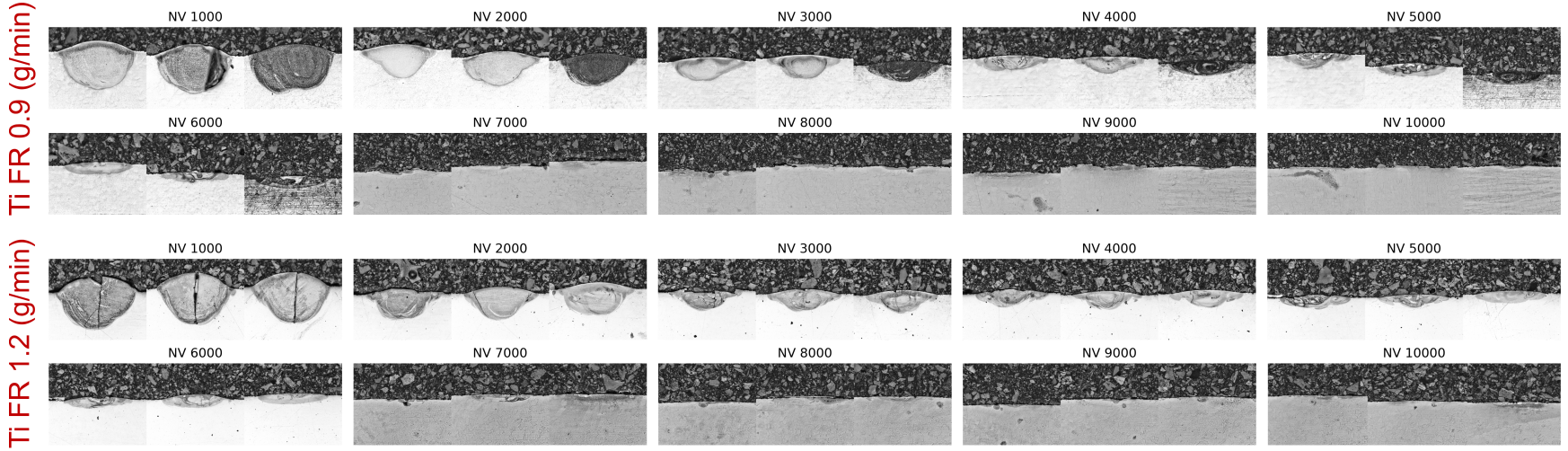

Figure 3: Metallographic summary of all rescanned tracks (R1) with varying Ti injection feed rates.

Appendix B

Code Examples

Code 1 : G-code for bidirectional steel block gcode

```
P1
N10 (**** Nozzle velocity ****)
*N20 P102 = 1000
N30 (**** Laser Power****)
*N40 P101 = 60
*N50 P101 = P101 * 1000
N60 G110 X0 Y0 Z0 B0 C0
N70 G111 V100 F50
N80 G112 V = P101 F = P102
N90 U20
N100
N110 (Block length)
*N120 P103 = 10
*N130 P103 = P103 * 1000
N140 (Height in number of layers)
*N150 P104 = 50
N160 (Width in number of lines)
*N170 P105 = 10
N180 (DELTA Z)
*N190 P106 = 0.2
*N200 P106 = P106 * 1000
N210 (DELTA XY)
*N220 P107 = 0.5
*N230 P107 = P107 * 1000
N240
N250 (**** Gas set up ****)
N260 M80
N270 M82
N280 (**** Powder set up ****)
N290 (* Feeder 2 *)
*N300 P63 = 7.5
*N310 P64 = 30
*N320 P65 = 20
N330 M64
N340 M66
N350 G4 F20000
N360
*N370 P108 = 0
*N380 P109 = 0
N390 G54
N400 G90
N410 G1 X0 Y0 Z0 B0 C0 F = P102
N420 G91
N430
N440 G1 Y = -P103 F = P102 M111
```

```
N450 G1 X = P107 M101
N460 G1 Y = P103 M111
N470 G1 X = P107 M101
*N480 P108 = P108 + 1
*N490 IF P108 < P105 GO 440
N500 G1 Z = P106
N510 G90
N520 G1 X0 Y0
N530 G91
*N540 P108 = 0
N550 G1 X = P103 F = P102 M111
N560 G1 Y = -P107 M101
N570 G1 X = -P103 M111
N580 G1 Y = -P107 M101
*N590 P108 = P108 + 1
*N600 IF P108 < P105 GO 550
N610 G1 Z = P106
N620 G90
N630 G1 X0 Y0
N640 G91
*N650 P109 = P109 + 1
*N660 P108 = 0
*N670 IF P109 < P104 GO 440
N680 M101
N690 M2
```

Code 2 : Batch CLAHE image processing java

```java
// Apply CLAHE to all images in a folder
// Save results to a chosen output folder.

dir = getDirectory("Choose a folder with input images");
outDir = getDirectory("Choose an output folder");
list = getFileList(dir);
setBatchMode(true); // speeds up processing by not updating display

for (i = 0; i < list.length; i++) {
    if (endsWith(list[i], ".jpg") || endsWith(list[i], ".bmp")) {
        open(dir + list[i]);
        // Convert to 8-bit
        run("8-bit");
        // Apply CLAHE
        run("Enhance Local Contrast (CLAHE)", "blocksize=127 histogram=256 maximum=3");
        // Save as TIFF
        saveAs("Tiff", outDir + list[i]);
        close();
    }
}
setBatchMode(false);
print("Done!");
```

Bibliography

[1] C. W. Hull. "Apparatus for production of three-dimensional objects by stereolithography". Patent US4575330A (United States). Mar. 1986 (cit. on p. 1).

[2] W. E. Frazier. "Metal Additive Manufacturing: A Review". In: *Journal of Materials Engineering and Performance* 23.6 (June 2014), pp. 1917–1928 (cit. on pp. 1, 3, 6).

[3] AMPOWER GmbH. KG. *Metal Additive Manufacturing: Technology overview*. Accessed: 2025-02-17. 2024. URL: `https://ampower.eu/infographics/metal-additive-manufacturing/` (cit. on p. 1).

[4] T. DebRoy et al. "Additive manufacturing of metallic components – Process, structure and properties". In: *Progress in Materials Science* 92 (2018), pp. 112–224 (cit. on pp. 2, 3, 6, 9, 10, 14, 41).

[5] A. Dass and A. Moridi. "State of the Art in Directed Energy Deposition: From Additive Manufacturing to Materials Design". In: *Coatings* 9.7 (2019) (cit. on pp. 2, 4, 6, 10).

[6] F. Martina et al. "Tandem Metal Inert Gas process for high productivity Wire Arc Additive Manufacturing in stainless steel". In: *Additive Manufacturing* 25 (Nov. 2018) (cit. on p. 3).

[7] K. Ribeiro et al. "A Study of Different Deposition Strategies in Direct Energy Deposition (DED) Processes". In: *Procedia Manufacturing* 48 (Jan. 2020), pp. 663–670 (cit. on pp. 4, 6).

[8] Z.D. Wang et al. "Investigation of the underwater laser directed energy deposition technique for the on-site repair of HSLA-100 steel with excellent performance". In: *Additive Manufacturing* 39 (2021), p. 101884 (cit. on p. 4).

[9] J.P. Kelly et al. "Directed energy deposition additive manufacturing of functionally graded Al-W composites". In: *Additive Manufacturing* 39 (2021), p. 101845 (cit. on p. 4).

[10] D. Singh, S. Arjula, and A. Raji. "Functionally Graded Materials Manufactured by Direct Energy Deposition: A review". In: *Materials Today: Proceedings* 47 (2021). International Conference on Materials and System Engineering, pp. 2450–2456 (cit. on p. 4).

[11] U. Articek et al. "Synthesis of functionally graded material H13/Cu by LENS technology". In: *Advances in Production Engineering & Management* 8 (Sept. 2013), pp. 169–176 (cit. on pp. 4, 6).

[12] P. Kürnsteiner et al. “High-strength Damascus steel by additive manufacturing”. In: *Nature* 582.7813 (June 2020), pp. 515–519 (cit. on p. 4).

[13] C. J. Todaro et al. “Grain structure control during metal 3D printing by high-intensity ultrasound”. In: *Nature Communications* 11.1 (Jan. 2020), p. 142 (cit. on pp. 4, 6, 10).

[14] W. Zhai, W. Zhou, and S. M. Ling Nai. “Grain refinement of 316L stainless steel through in-situ alloying with Ti in additive manufacturing”. In: *Materials Science and Engineering: A* 840 (2022), p. 142912 (cit. on pp. 5, 13–16, 34).

[15] Z. Kerneret al. “Comparative electrochemical study of 08H18N10T, AISI 304 and AISI 316L stainless steels”. In: *Electrochimica Acta* 52.27 (2007), pp. 7529–7537 (cit. on pp. 5, 14).

[16] D. D’Andrea. “Additive Manufacturing of AISI 316L Stainless Steel: A Review”. In: *Metals* 13.8 (2023) (cit. on p. 5).

[17] A. Aversa, G. Marchese, and E. Bassini. “Directed Energy Deposition of AISI 316L Stainless Steel Powder: Effect of Process Parameters”. In: *Metals* 11.6 (2021) (cit. on pp. 6, 38, 41, 46).

[18] Z. Wang, T.A. Palmer, and A. M. Beese. “Effect of processing parameters on microstructure and tensile properties of austenitic stainless steel 304L made by directed energy deposition additive manufacturing”. In: *Acta Materialia* 110 (2016), pp. 226–235. ISSN: 1359-6454 (cit. on pp. 6, 16).

[19] L. Gao et al. “Tailoring material microstructure and property in wire-laser directed energy deposition through a wiggle deposition strategy”. In: *Additive Manufacturing* 77 (2023), p. 103801 (cit. on pp. 6, 14).

[20] Y. Wang et al. “Microstructure and mechanical properties of TiN particles strengthened 316L steel prepared by laser melting deposition process”. In: *Materials Science and Engineering: A* 814 (2021), p. 141220 (cit. on pp. 6–8, 21, 55).

[21] Q. Tan et al. “Unravelling the roles of TiN-nanoparticle inoculant in additively manufactured 316 stainless steel”. In: *Journal of Materials Science & Technology* 175 (2024), pp. 153–169 (cit. on pp. 6, 7, 10, 11, 16–18, 21, 53, 55).

[22] H. Ikehata, D. Mayweg, and E. Jägle. “Grain refinement of Fe–Ti alloys fabricated by laser powder bed fusion”. In: *Materials & Design* 204 (2021), p. 109665 (cit. on pp. 7, 11, 21, 51, 52).

[23] Sindo Kou. *Welding Metallurgy*. 2nd. Hoboken: Wiley, 2003, pp. 145–197 (cit. on pp. 9, 10, 12, 14, 37).

[24] S. Petrovič et al. “Differential scanning calorimetry study of the solidification sequence of austenitic stainless steel”. In: *Journal of Thermal Analysis and Calorimetry* 105 (July 2011), pp. 251–257 (cit. on p. 9).

[25] S. Li et al. “Directed energy deposition of metals: processing, microstructures, and mechanical properties”. In: *International Materials Reviews* 68.6 (2023), pp. 605–647 (cit. on p. 10).

[26] M. Gäumann, R. Trivedi, and W. Kurz. “Nucleation ahead of the advancing interface in directional solidification”. In: *Materials Science and Engineering: A* 226-228 (1997). Ninth International Conference on Rapidly Quenched and Metastable Materials, pp. 763–769. ISSN: 0921-5093 (cit. on pp. 10, 11).

[27] A. Durga et al. “Grain refinement in additively manufactured ferritic stainless steel by in situ inoculation using pre-alloyed powder”. In: *Scripta Materialia* 194 (2021), p. 113690 (cit. on pp. 10, 18, 21, 41).

[28] WC. Winegard and B. Chalmers. “Supercooling and dendritic freezing in alloys”. In: *Transactions of the American Society for Metals* 46 (1954), pp. 1214–1224 (cit. on pp. 11, 13).

[29] D.H. StJohn et al. “The Interdependence Theory: The relationship between grain formation and nucleant selection”. In: *Acta Materialia* 59.12 (2011), pp. 4907–4921 (cit. on pp. 11, 13, 14).

[30] Y. Xu and et al. “Revealing the heterogeneous nucleation behavior of equiaxed grains of inoculated Al alloys during directional solidification”. In: *Acta Materialia* 149 (2018), pp. 312–325 (cit. on p. 11).

[31] Q. Tan, Y. Yin, and M.X. Zhang. “Comparison of the Grain-Refining Efficiencies of Ti and LaB6 Inoculants in Additively Manufactured 2024 Aluminum Alloy: The Important Role of Solutes”. In: *Metals* 13.8 (2023) (cit. on pp. 11, 14).

[32] W. Kurz, D. Fisher, and M. Rappaz. *Fundamentals of Solidification, Fifth Revised Edition*. Switzerland: Trans Tech Publications Ltd., Apr. 2023 (cit. on pp. 11, 13).

[33] M. Gäumann, S. Henry, F. Cléton, J.D. Wagnière, and W. Kurz. “Epitaxial laser metal forming: analysis of microstructure formation”. In: *Materials Science and Engineering: A* 271.1 (1999), pp. 232–241 (cit. on p. 11).

[34] Q. Tan et al. “Demonstrating the roles of solute and nucleant in grain refinement of additively manufactured aluminium alloys”. In: *Additive Manufacturing* 49 (2022), p. 102516 (cit. on pp. 13–15).

[35] A. Prasad et al. “Towards understanding grain nucleation under Additive Manufacturing cation conditions”. In: *Acta Materialia* 195 (2020), pp. 392–403 (cit. on p. 14).

[36] Q. Tan et al. “Simultaneous enhancements of strength and ductility of a selective laser melted H13 steel through inoculation treatment”. In: *Scripta Materialia* 219 (2022), p. 114874 (cit. on p. 16).

[37] K. Mo. “Study on the microstructure and wear resistance of laser clad martensitic stainless steel 420 with different content of TiC”. In: *Materials Today Communications* 46 (2025), p. 112615 (cit. on pp. 16, 55).

[38] Y. Ozawa and K. Mori. “Critical Condition for Penetration of Solid Particle into Liquid Metal”. In: *Transactions of the Iron and Steel Institute of Japan* 23.9 (1983), pp. 769–774 (cit. on pp. 19, 20).

[39] O. Verezub et al. “In-situ synthesis of a carbide reinforced steel matrix surface nanocomposite by laser melt injection technology and subsequent heat treatment”. In: *Surface and Coatings Technology* 203.20 (2009), pp. 3049–3057 (cit. on pp. 19, 20).

[40] A. Aggarwal, V. Pandiyan, C. Leinenbach, and M. Leparoux. “Investigating laser beam shadowing and powder particle dynamics in directed energy deposition through high-fidelity modelling and high-speed imaging”. In: *Additive Manufacturing* 91 (2024), p. 104344 (cit. on pp. 20, 46, 48, 49, 58).

[41] X. Changji et al. “Wettability of TiN by Liquid Iron and Steel”. In: *ISIJ International* 55 (Sept. 2015), pp. 1642–1651 (cit. on p. 20).

[42] J. Yang, L. M. Schlenger, M. H. Nasab, St. Van Petegem, F. Marone, R. E. Logé, and C. Leinenbach. “Experimental Quantification of Inward Marangoni Convection and Its Impact on Keyhole Threshold in Laser Powder Bed Fusion of Stainless Steel”. In: *Additive Manufacturing* 84 (2024), p. 104092 (cit. on pp. 20, 21, 46, 50, 51, 58).

[43] Z. Saldi et al. “Effect of enhanced heat and mass transport and flow reversal during cool down on weld pool shapes in laser spot welding of steel”. In: *International Journal of Heat and Mass Transfer* 66 (Sept. 2013), pp. 879–888 (cit. on pp. 20, 50, 51).

[44] L. Aucott et al. “Revealing internal flow behaviour in arc welding and additive manufacturing of metals”. In: *Nature Communications* 9.1 (Dec. 2018), p. 5414. ISSN: 2041-1723 (cit. on pp. 20, 50, 51).

[45] ASTM International. *Standard Specification for Titanium and Titanium Alloy Bars and Billets*. `https://www.astm.org/standards/b348`. Accessed: 2025-06-06 (cit. on p. 22).

[46] AP&C a Colibrium Additive company. *Commercially Pure Titanium Cp-Ti Grade 1*. `https://www.advancedpowders.com/powders/titanium-alloys/cp-ti-grade-1`. Accessed: 2025-06-06 (cit. on pp. 22, 23).

[47] Y. Yang et al. “Densification, mechanical behaviors, and machining characteristics of 316L stainless steel in hybrid additive/subtractive manufacturing”. In: *The International Journal of Advanced Manufacturing Technology* 107 (2020), pp. 177–189 (cit. on p. 28).

[48] K. Zuiderveld. “Contrast limited adaptive histogram equalization”. In: *Graphics Gems IV*. USA: Academic Press Professional, Inc., 1994, pp. 474–485 (cit. on p. 30).

[49] V. Lindström et al. “Laser Powder Bed Fusion of Metal Coated Copper Powders”. In: *Materials* 13.16 (2020) (cit. on p. 50).